This is an open access article published under a Creative Commons Non-Commercial No Derivative Works (CC-BY-NC-ND) Attribution License, which permits copying and redistribution of the article, and creation of adaptations, all for non-commercial purposes.

THE JOURNAL OF PHYSICAL CHEMISTRY C

Article

Cite This: J. Phys. Chem. C 2019, 123, 8484−8499

pubs.acs.org/JPCC

Electronic Structure of Lanthanide-Doped Bismuth Vanadates: A Systematic Study by X-ray Photoelectron and Optical Spectroscopies

Matthew D. M. Robinson,[†] Freddy E. Oropeza,[*,†,‡] Meiyan Cui,[§] Kelvin H. L. Zhang,[*,§] Mareike V. Hohmann,[†,∥] David J. Payne,[⊥] Russell G. Egdell,[†] and Anna Regoutz[⊥]

[†]Department of Chemistry, Inorganic Chemistry Laboratory, University of Oxford, South Parks Road, Oxford OX1 3QR, U.K.

[‡]Laboratory of Inorganic Materials and Catalysis, Department of Chemical Engineering and Chemistry, Eindhoven University of Technology, P.O. Box 513, Eindhoven 5600 MB, The Netherlands

[§]State Key Laboratory of Physical Chemistry of Solid Surfaces, College of Chemistry and Chemical Engineering, Xiamen University, Xiamen 361005, People's Republic of China

[∥]Institute of Materials Science, Surface Science Division, Technische Universität Darmstadt, Darmstadt 64287, Germany

[⊥]Department of Materials, Imperial College London, Exhibition Road, London SW7 2AZ, U.K.

Supporting Information

ABSTRACT: Monoclinic $BiVO_4$ has emerged in recent years as one of the most promising materials for photocatalytic evolution of oxygen under solar irradiation. However, it is in itself unable to phototcatalyze reduction of water to hydrogen due to the placement of the conduction band edge below the potential required for H_2O/H_2 reduction. As a consequence, $BiVO_4$ only finds application in a hybrid system. Very recently, tetragonal lanthanide-doped $BiVO_4$ powders have been shown to be able to both reduce and to oxidize water under solar irradiation, but to date there has been no comprehensive study of the electronic properties of lanthanide-doped bismuth vanadates aimed at establishing the systematic trends in the electronic structure in traversing the lanthanide series. Here, the accessible family of lanthanide-doped $BiVO_4$ quaternary oxides of stoichiometry $Bi_{0.5}Ln_{0.5}VO_4$ (Ln = La to Lu, excluding Pm) has been studied by X-ray powder diffraction, X-ray photoemission spectroscopy, and diffuse reflectance optical spectroscopy. The compounds all adopt the tetragonal zircon structure, and lattice parameters decrease monotonically in traversing the lanthanide series. At the same time, there is an increased peak broadening in the diffraction patterns as the mismatch in ionic radius between Bi^{3+} and the Ln^{3+} ions increases across the series. Valence band X-ray photoemission spectra show that the final state $4f^{n-1}$ structure associated with ionization of lanthanide $4f^n$ states is superimposed on the valence band structure of $BiVO_4$ in the quaternary materials: in the case of the Ce-, Pr- and Tb-doped $BiVO_4$, 4f-related states appear above the top of the main valence band of $BiVO_4$ and account for the small bandgap in the Ce compound. In all cases, the 4f structure is characteristic of the lanthanide element in the Ln(III) oxidation state. Vanadium 2p and lanthanide 3d or 4d core level photoelectron spectra of those compounds where the lanthanide may in principle adopt a higher (Ln = Ce, Pr, Tb) or lower (Ln = Eu, Yb) oxidation state further confirm the prevalence of the Ln(III) valence state throughout. The visible region optical properties of all samples were studied by diffuse reflectance spectroscopy, with a particular focus on the optical bandgap and the details of transitions associated with localized 4f states. Taken together, the results demonstrate the remarkable tunability of optical and electronic properties for these quaternary materials.

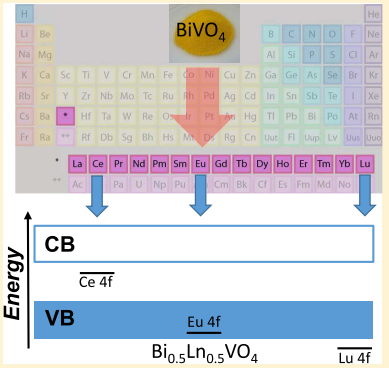

1. INTRODUCTION

Photocatalytic splitting of water into hydrogen and oxygen under solar irradiation is one of the most promising ways of harnessing energy from the sun to produce a nonpolluting and transportable fuel. Photoelectrolytic decomposition of water in an electrochemical cell incorporating a TiO_2 anode and a platinum cathode was first reported in 1972,[1] followed in 1977 by water splitting on a powder TiO_2 photocatalyst suspended in water under ultraviolet irradiation.[2] Since then, many other oxide photocatalytic materials have been investigated.[3] A minimum bandgap of 1.23 eV is required for water splitting. In addition, the conduction band edge must lie above the potential for reduction of water to hydrogen by electrons photoexcited into the conduction band, whereas the valence band edge must lie below the potential for oxygen evolution so that the photoholes can oxidize water. In optimizing solar-

Received: October 30, 2018
Revised: March 5, 2019
Published: March 6, 2019

Downloaded via IMPERIAL COLLEGE LONDON on April 17, 2019 at 11:00:11 (UTC).
See https://pubs.acs.org/sharingguidelines for options on how to legitimately share published articles.

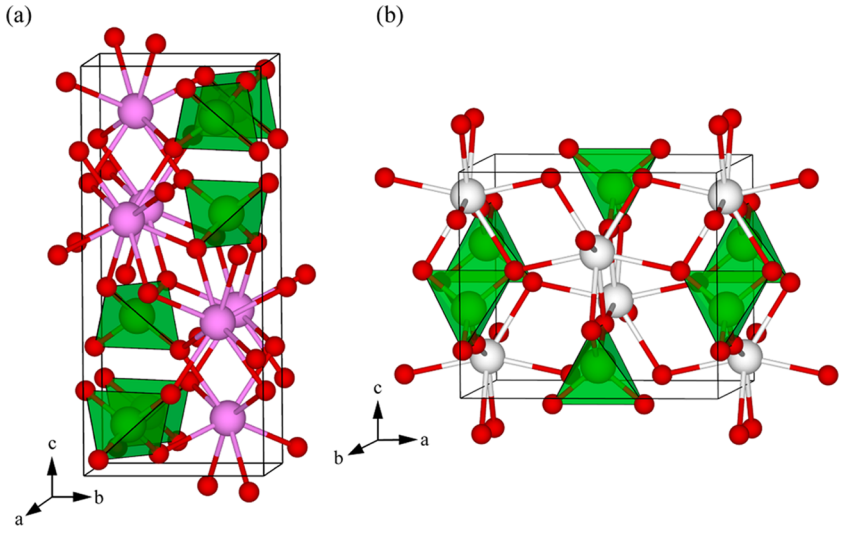

Figure 1. (a) Structure of monoclinic $BiVO_4$. (b) The tetragonal zircon structure adopted by $LnVO_4$ (Ln = lanthanide). Bi atoms pink; Ln atoms gray; O atoms red; VO_4 tetrahedra highlighted in green.

driven photocatalysts, there is a trade-off between increasing the overpotential for the production of hydrogen and oxygen by widening the bandgap above the minimum value and keeping the fraction of the visible spectrum that is absorbed as high as possible. An alternative strategy is to combine two different photocatalytic materials, one optimized for hydrogen evolution and one for oxygen evolution, in a so-called Z-scheme system.[4,5] Finally, a catalytically active photoanode may be used in tandem with a photovoltaic cell in a hybrid photoelectrochemical reactor.[6]

After the discovery that monoclinic $BiVO_4$ is an efficient photocatalyst for oxygen evolution in 1999,[7] there has been an ongoing interest in improving the performance of this particular material, as detailed in two recent review articles.[8,9] Well, over 1200 papers published in the past 20 years have $BiVO_4$ in the title, most concerned with photocatalysis. Recent developments include improvement of the oxygen quantum yield by optimizing the morphology of $BiVO_4$ nanoparticles to include a large fraction of high index surfaces;[10] the use of $BiVO_4$ as an anode or sensitizer in a photoelectrochemical cell;[11−13] photovoltaic devices including $BiVO_4$ as an active layer;[14,15] and tandem photoelectrochemical devices including a $BiVO_4$ photoanode and a photovoltaic cell to enhance water splitting. The solar cells that have been in use in this way include conventional Si solar cells,[16−19] III−V cells based on $GaAs/Ga_{1-x}In_xAs_{1-x}P_x$,[20] and recently developed perovskite solar cells.[21]

$BiVO_4$ has three different polymorphs:[22] orthorhombic pucherite,[23] tetragonal dreyerite,[24] and monoclinic clinobisvanite.[25] The monoclinic phase is most stable thermodynamically at room temperature and also displays the most promising photocatalytic activity. This phase belongs to space group $C2/c$ and contains BiO_8 polyhedra and VO_4 tetrahedra, as shown in Figure 1.[25] The polyhedra around the Bi atoms are significantly distorted with four different bond lengths: 2 × 2.346, 2 × 2.375, 2 × 2.528, and 2 × 2.605 Å. This creates a weakly layered ferroelectric structure stacked in the c direction with the bonds shorter than 2.4 Å on one side of the Bi ions and those longer than 2.5 Å on the other. The coordination geometry is suggestive of stereochemically active Bi(III) lone pairs, arising from fully occupied Bi 6s states lying well below the bottom of the O 2p valence band which hybridize with O 2p states to give Bi 6s−O 2p antibonding states at the top of the valence band. These further hybridize with nominally empty 6p states to give the directional lone pairs.[26−29] Early calculations suggested that the monoclinic $BiVO_4$ had an unusual band structure, the lowest energy (2.5 eV) direct transitions being found away from Γ at the A point.[30] However, recent experimental evidence points to an indirect gap of 2.52 eV, with a direct gap of 2.68 eV,[31] in broad agreement with more refined calculations.[32−34] Tetragonal $BiVO_4$ adopts the zircon structure (space group $I4_1/amd$) and is generally believed to have a much larger gap of about 2.9 eV,[8] although a smaller value of 2.7 eV was reported recently.[35] Its structure is again based on VO_4 tetrahedra and BiO_8 polyhedra, but the latter is more regular than in the monoclinic phase, and as shown in Figure 1 have approximate D_{2d} symmetry. This tetragonal zircon structure is also adopted by lanthanide vanadates $LnVO_4$.

Monoclinic $BiVO_4$ is generally reported to be the most active phase in photocatalytic applications. Nonetheless, the conduction band edge for monoclinic $BiVO_4$ lies below the electrochemical potential for production of hydrogen and limits the application of this oxide to composite Z schemes, where a second photocatalytic material is required for hydrogen evolution;[36] or as discussed above to hybrid photoelectrolytic reactors incorporating a photovoltaic cell to provide an additional deriving potential for hydrogen evolution. Alternatively, oxygen is evolved in the presence of a sacrificial species such as Ag^+, which is more easily reduced than water.[7] However, the quaternary lanthanide-doped bismuth vanadates $Bi_{0.5}La_{0.5}VO_4$,[37] $Bi_{0.5}Dy_{0.5}VO_4$,[38] and $Bi_{0.5}Gd_{0.5}VO_4$[39] have been shown to function as catalysts for evolution of both oxygen and hydrogen in a simple water splitting photochemical reaction: the range of was later extended to a wider range of dopants including Nd, Sm, and Eu.[40] The photocatalytic activity of monoclinic $BiVO_4$ "loaded" with 8% of a series of lanthanide oxides has also been studied, optimal performance being obtained with the Gd-loaded material.[41] Lanthanide doping generally tips $BiVO_4$ toward the tetragonal phase, and the associated widening of the bandgap is undoubtedly one factor favouring water

DOI: 10.1021/acs.jpcc.8b10573
J. Phys. Chem. C 2019, 123, 8484−8499

splitting. However, further effects such as changes in particle size and morphology and inhibition of electron−hole recombination by lanthanide dopants are probably also important in improving the photocatalytic performance of Gd-doped $BiVO_4$ in degradation of rhodamine B dye[42] and of enhancing the performance of Er/Y co-doped $BiVO_4$ in the photoinactivation of *Escherichia coli* bacteria.[43]

In a different context, Eu-doped $BiVO_4$ has attracted recent attention as materials for phosphor applications,[35] whereas Tm/Yb- co-doped $BiVO_4$ is of interest for up-conversion photoluminescence, whereby red emission from Tm^{3+} is produced under near-infrared (NIR) excitation of the $^2F_{7/2} \rightarrow {}^2F_{5/2}$ transition in Yb^{3+}.[44,45] Up-conversion has also been used to promote photocatalytic degradation of methylene blue under NIR irradiation using a Yb/Er/Tm co-doped $BiVO_4$ catalyst[46] and to increase the rate of photodegradation of rhodamine B by Nd/Er co-doped $BiVO_4$.[47]

Against this background, it is surprising that there has to date been no systematic study of the electronic properties of doped bismuth vanadate solid solutions across the whole lanthanide. Here, we present a study of all 14 accessible quaternary compounds of general formula $Bi_{0.5}Ln_{0.5}VO_4$ (Ln = lanthanide), owing to the highly radioactive nature of promethium, this lanthanide could not be included. As mentioned above, the parent lanthanide vanadates themselves adopt a tetragonal zircon structure based on vanadate tetrahedra and almost-regular lanthanide LnO_8 polyhedra, with two Ln−O bond lengths that typically differ by about 0.1 Å.[48−51] As a preliminary to preparation of a complete series of quaternary compounds, we explored the phases formed by high-temperature reaction between Bi_2O_3, Dy_2O_3 and V_2O_5 to give $Bi_{1-x}Dy_xVO_4$ solid solutions with x values between 0 and 1. Although mixed phase material was obtained for $x \leq 0.3$, only the tetragonal phase was formed when $x \geq 0.4$. It was then possible to prepare a tetragonal zircon phase $Bi_{0.5}Ln_{0.5}VO_4$ for all of the lanthanides. X-ray diffraction confirmed that the lattice parameters decreased in a monotonic fashion across the lanthanide series, although the changes were lower than for the parent $LnVO_4$ compounds.[49−51] Pronounced peak broadening was found toward the end of the quaternary series, perhaps indicating incipient spinodal decomposition as the size mismatch between Bi^{3+} and Ln^{3+} increases.

Valence and core level X-ray photoemission spectroscopy (XPS) was used to probe the valence states of the lanthanide elements and the location of 4f states relative to the main valence band of $BiVO_4$. The XPS results provide a basis for understanding anomalously low bandgap found in diffuse reflectance optical spectra of $Bi_{0.5}Ce_{0.5}VO_4$. Finally, diffuse reflectance spectroscopy allows us to identify those compounds where strong 4f transitions are found in the visible region; and to establish that the energies of the 4f transitions may be tuned to some extents by varying the composition of $Bi_{1-x}Ln_xVO_4$ solid solutions.

2. EXPERIMENTAL SECTION

Quaternary solid solutions of composition $Bi_{0.5}Ln_{0.5}VO_4$ were prepared by ceramic solid synthesis. Bi_2O_3 (Sigma-Aldrich 99.999%), Ln_2O_3 (Sigma-Aldrich 99.99%, where Ln is a lanthanide between Nd and Lu, excluding Pm), and V_2O_5 (Sigma-Aldrich 99.99%) were ground in an agate mortar and pestle in appropriate stoichiometric quantities, pelletized between 13 mm diameter tungsten carbide dies under a 5 ton loading for 5 min and then fired at 600 °C for 16 h. CeO_2 (Sigma-Aldrich 99.99%) and Pr_6O_{11} (Sigma-Aldrich 99.99%) were used instead of the sesquioxides in the preparation of $Bi_{0.5}Ce_{0.5}VO_4$ and $Bi_{0.5}Pr_{0.5}VO_4$. The products of the initial firing were reground and refired at 900 °C for an additional 16 h. Further samples of $Bi_{1-x}Dy_xVO_4$ with $0 < x < 1$ were prepared by adjusting the stoichiometry in the starting mixture. The final ceramic pellets were reground prior to measurement of $\theta-2\theta$ X-ray powder diffraction patterns in a PANalytical X'Pert diffractometer incorporating a monochromated Cu Kα source.

X-ray photoemission spectra were measured in a Scienta ESCA 300 spectrometer housed in Daresbury Laboratory U.K. This incorporates a rotating anode Al Kα ($h\nu$ = 1486.6 eV) X-ray source, a seven-crystal X-ray monochromator, and a 300 mm mean radius spherical sector electron energy analyzer with parallel electron detection using channel plates, a scintillation screen, and a camera. The X-ray source was run with 200 mA emission current and 14 kV anode bias, whereas the analyzer operated at 150 eV pass energy. Gaussian convolution of the analyzer resolution with a linewidth of 260 meV for the X-ray source gives an effective instrument resolution of 400 meV. Binding energies are referenced to the Fermi energy of a silver sample regularly used to calibrate the spectrometer.

Diffuse reflectance spectra in the wavelength range between 250 and 800 nm were measured using a PerkinElmer Lamda 750S ultraviolet/visible spectrometer incorporating a 60 mm integrating sphere.

3. RESULTS AND DISCUSSION

3.1. X-ray Diffraction. In a preliminary set of experiments, the phases formed by high-temperature reaction between the precursors Bi_2O_3, Dy_2O_3, and V_2O_5 were explored as a function of composition in $Bi_{1-x}Dy_xVO_4$. As shown in Figure 2, for $x = 0.05$, the monoclinic structure of $BiVO_4$ is retained, whereas for $0.1 \leq x \leq 0.3$, a mixture of monoclinic and tetragonal phases is obtained. For $x \geq 0.4$, the monoclinic phase is absent, and only the tetragonal zircon phase is found. The full indexed diffraction pattern of $Bi_{0.5}Dy_{0.5}VO_4$ is shown in Figure 3, where it is compared to that for the parent ternary compound $DyVO_4$. All of the peaks match, although there is a pronounced shift to a low angle for peaks in the powder pattern of $Bi_{0.5}Dy_{0.5}VO_4$. The peaks are also broader for the quaternary material, as emphasized in the bottom panel of Figure 3.

These findings prompted us to attempt to prepare the complete series of ternary compounds $Bi_{0.5}Ln_{0.5}VO_4$, where Ln ranges between La and Lu. Diffraction patterns of two compounds toward the beginning ($Bi_{0.5}Ce_{0.5}VO_4$) and the end ($Bi_{0.5}Lu_{0.5}VO_4$) of the series are shown in Figure 4, along with expansions across the (112) reflection.

The complete set of diffraction patterns is given as the Supporting Information (Figure S1). A pronounced shift to high angle is evident in comparing the Ce and Lu compounds, along with very pronounced broadening of the diffraction peaks in traversing the lanthanide series, in fact, the (112) peak for $Bi_{0.5}Lu_{0.5}VO_4$ shows incipient splitting into two components.

The major trends in the diffraction patterns are summarized in Figure 5, which shows variations in the a and c lattice parameters, in the ratio c/a and in the full width at half maximum height (FWHM) for the (112) reflection. Numerical values for the lattice parameters are given as the Supporting

DOI: 10.1021/acs.jpcc.8b10573
J. Phys. Chem. C 2019, 123, 8484−8499

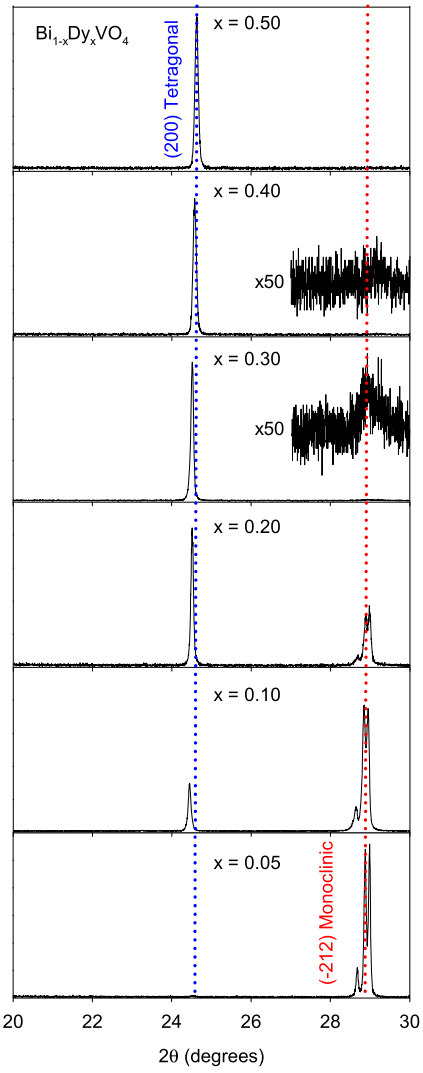

Figure 2. θ–2θ X-ray diffraction patterns of ceramic $Bi_{1-x}Dy_xVO_4$ in the 2θ range between 20 and 30° as a function of composition parameter x, showing the emergence of the tetragonal phase and disappearance of the monoclinic phase as x increases.

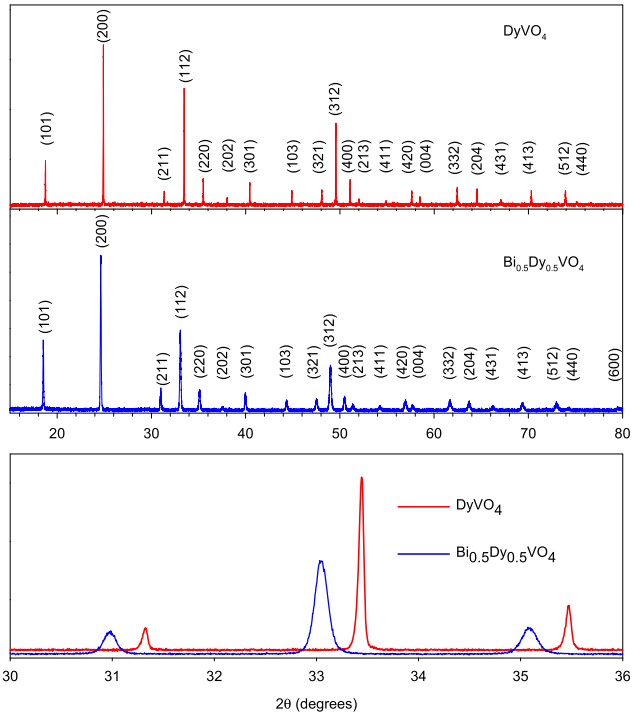

Figure 3. θ–2θ X-ray diffraction patterns of tetragonal $DyVO_4$ and $Bi_{0.5}Dy_{0.5}VO_4$ with the reflections all labeled. The lower panel shows the 2θ region between 30 and 36°, emphasizing the shift to the low angle between $DyVO_4$ and $Bi_{0.5}Dy_{0.5}VO_4$.

Information (Table S1). Comparative data for a, c, and c/a for the $LnVO_4$ series are also plotted. Both a and c decrease across the lanthanide series as the ionic radius for the eight-coordinate lanthanide cation decreases from 1.160 Å for La^{3+} to 0.977 Å for Lu^{3+}.[52] As expected, the changes are more pronounced for the parent ternary compounds, where $\Delta a/a(LnVO_4)$ = 5.79% and $\Delta c/c(LnVO_4)$ = 4.79%,[49−51] than for the quaternary solid solutions, where $\Delta a/a(Bi_{0.5}Ln_{0.5}VO_4)$ = 3.25% and $\Delta c/c(Bi_{0.5}Ln_{0.5}VO_4)$ = 2.47%. In both series, the decrease in c is less than the change in a, so the ratio c/a increases. The standard tabulation of ionic radii due to Shannon gives an ionic radius for Bi^{3+} of 1.17 Å; this is bigger than for all of the lanthanides, including La^{3+} itself.[52] It might, therefore, be expected that the lattice parameters for all of the $LnVO_4$ compounds should be smaller than for the corresponding $Bi_{0.5}Ln_{0.5}VO_4$ compounds. In fact, the lattice parameters are bigger for the parent vanadates of the early lanthanides, with a crossover in the a parameter between Nd and Sm and in the c parameter between Pr and Nd. This discrepancy has been discussed in detail previously in relation to the Ce compound[48] and probably reflects the difficulty in defining a transferable ionic radius for Bi^{3+}, which generally adopts low symmetry coordination environments. The current findings are in accord with lattice parameters for tetragonal $BiVO_4$ determined by Bhattacharya et al.[53] They found that a = 7.307 Å, intermediate between values for the Nd and Sm quaternaries (7.319 and 7.284 Å), respectively; and c = 6.466 Å, very close to the value of 6.462 Å for $Bi_{0.5}Pr_{0.5}VO_4$. Even though Bi^{3+} appears to have a smaller effective ionic radius in the tetragonal zircon phase than is usually assumed, the mismatch in radius between Ln^{3+} and Bi^{3+} obviously increases toward the end of the lanthanide series. The increased peak broadening from Gd^{3+} onward is suggestive of compositional inhomogeneity linked to this mismatch, and the incipient splittings of diffraction peaks mentioned above may be indicative of the onset of spinodal decomposition into Ln^{3+}- and Bi^{3+}-rich domains.

It is beyond the scope of the current paper to perform full structural refinements for all fourteen compound studied. However, Rietveld profile analysis was completed for two representative compounds—one near the start of the lanthanide series ($Bi_{0.5}Ce_{0.5}VO_4$) and one near the end ($Bi_{0.5}Tm_{0.5}VO_4$—Tm was selected rather than Yb or Lu since as discussed above the latter gave rather poor quality diffraction patterns with broad and asymmetric peaks). The results of the refinements are given as the Supporting Information (Table S2), where the comparison is made with structural data for $CeVO_4$ and $TmVO_4$.[50] The fitted profiles themselves are also given as the Supporting Information (Figure S2).

3.2. 4f Ionizations in Valence Region Photoelectron Spectra. Valence region photoelectron spectra of the series $Bi_{0.5}Ln_{0.5}VO_4$ (Ln = La to Lu, excluding Pm) are shown in Figure 6, scans extended to show shallow core levels are given as the Supporting Information (Figures S3 and S4). In broad

DOI: 10.1021/acs.jpcc.8b10573
J. Phys. Chem. C 2019, 123, 8484−8499

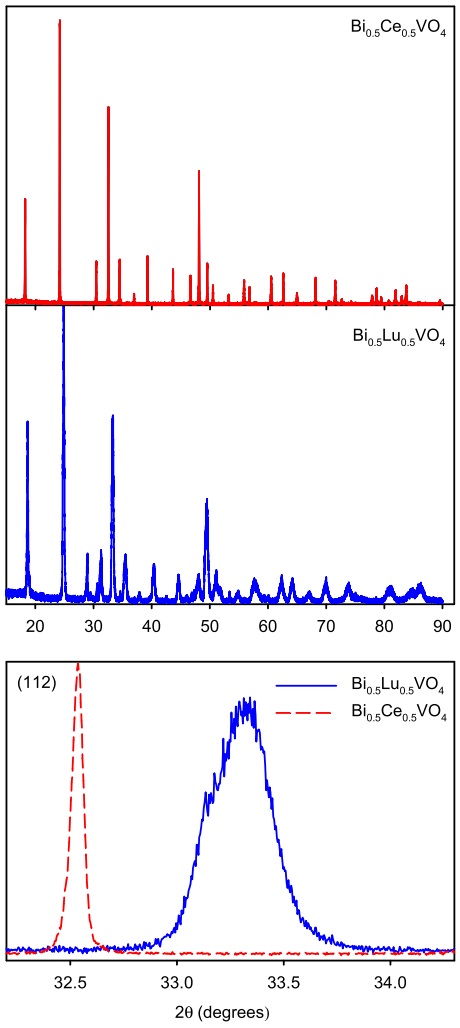

Figure 4. θ–2θ X-ray diffraction patterns of tetragonal $Bi_{0.5}Ce_{0.5}VO_4$ and $Bi_{0.5}Lu_{0.5}VO_4$. The lower panel shows expansions of scans across the (112) reflection, emphasizing the shift to high angle and broadening of the diffraction peaks in traversing the lanthanide series.

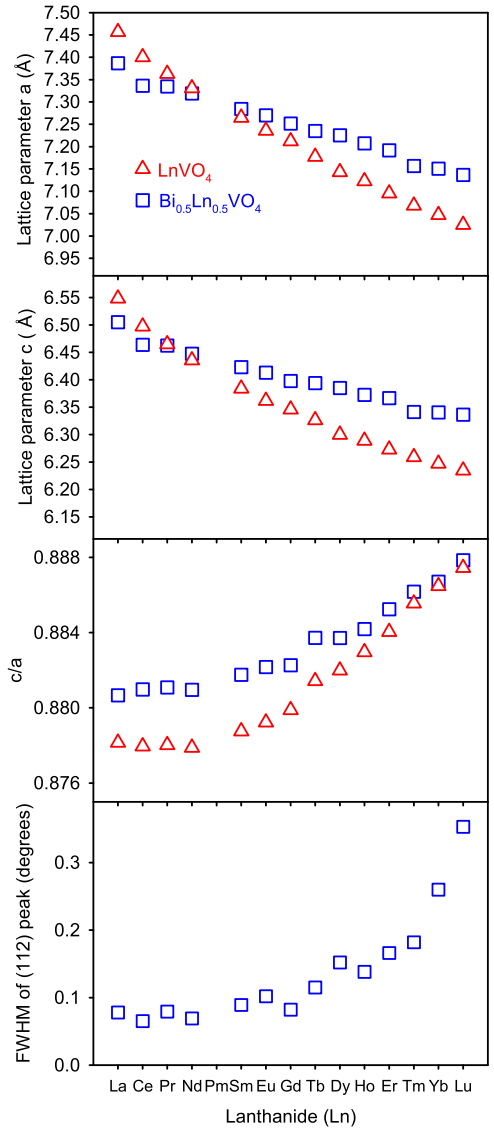

Figure 5. *a* and *c* lattice parameters for the complete (excluding Pm) series of tetragonal $Bi_{0.5}Ln_{0.5}VO_4$ (Ln = lanthanide) solid solutions, compared to published values for the $LnVO_4$.[50,51] The lower panels show the corresponding changes in the ratio *c*/*a* and the values and of full width at half maximum height of the (112) reflection for $Bi_{0.5}Ln_{0.5}VO_4$.

terms, the spectra become increasingly dominated by 4f ionizations as the f electron count increases from 0 for the La compound to 14 for the Lu compound. This is due both to the increasing occupancy of the 4f shell and the fact that the one-electron cross-section for ionization of a 4f electron increases from 1.1×10^{-3} Mb for Ce to 6.9×10^{-3} Mb for Lu.[54] These values are higher than for the other orbitals involved in the valence bands of these compounds, as summarized in Table 1. The $4f^n$ contribution to the spectra is determined not by the 4f PDOS but rather by the pattern of $4f^{n-1}$ final state multiplets that are reached upon ionizing the $4f^n$ configuration. The energies of the multiplets are determined by interelectron repulsion and spin–orbit coupling, whereas the probability of reaching a given multiplet is determined by coefficients of fractional parentage. These show how the $4f^n$ initial state can be expanded in terms of $4f^{n-1}$ final state wave functions coupled to f^1. More specifically, in the *LS* limit, the probability *P* of reaching a final state $(S'L'J')$ from an initial state (SLJ) for a $4f^n$ configuration can be written as[55,56]

$$P(S'L'J') = P(S'L')(2J' + 1)(2L + 1)(2S + 1) \times \left[6 \begin{pmatrix} 1/2 & S & S' \\ 3 & L & L' \\ 5/2 & J & J' \end{pmatrix}^2 + 8 \begin{pmatrix} 1/2 & S & S' \\ 3 & L & L' \\ 7/2 & J & J' \end{pmatrix}^2 \right] \quad (1)$$

where

$$P(S'L') = n\sigma_{i,4f} |\langle f^{n-1} S'L' f | \dagger \} f^n SL \rangle|^2 \quad (2)$$

In eq 1, the 3 × 3 terms in brackets are Wigner 9j symbols, whereas in eq 2, the $|\langle f^{n-1}S'L'f|\dagger\}f^nSL\rangle|$ are the coefficients of fractional parentage. These ideas were extended by Gerken to deal with the intermediate coupling, which allows excited states with different spin multiplicities to mix with the Russell–Saunders ground term, provided the states have the same *J* value, although this mixing is generally quite weak.[57] Gerken

DOI: 10.1021/acs.jpcc.8b10573
J. Phys. Chem. C 2019, 123, 8484–8499

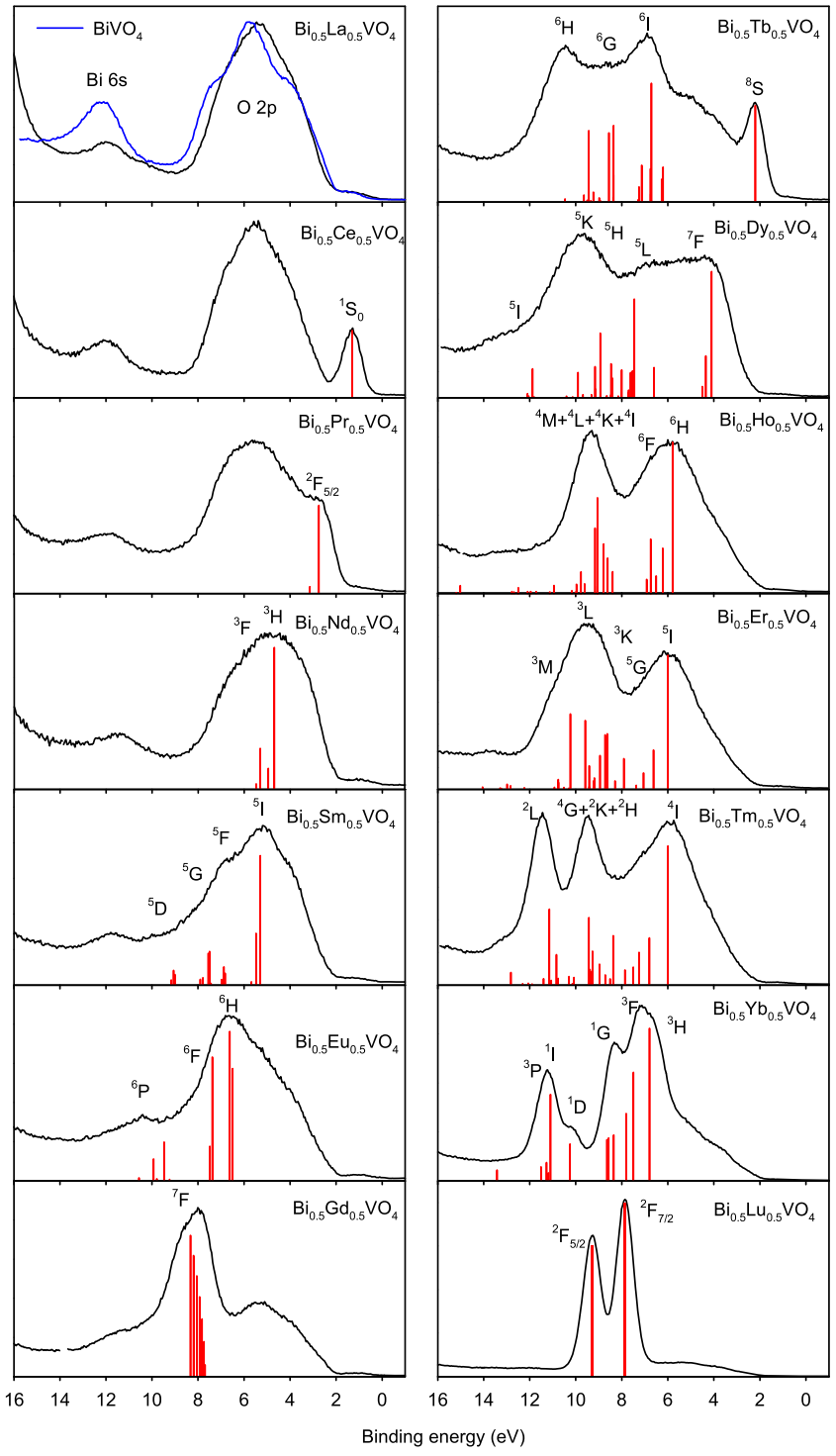

Figure 6. Valence band X-ray photoemission spectra of $Bi_{0.5}Ln_{0.5}VO_4$ (Ln = lanthanide, excluding Pm) solid solutions. The positions and intensities of final state components arising from 4f ionization as calculated by Gerken[57] are shown in red below the experimental spectra, with a rigid shift to align the peaks (the lowest energy state in Gerken's calculations is always set at zero binding energy). The major states arising from ionization from occupied $4f^n$ configurations are labeled, but it is not possible in a diagram of this sort to identify all of the components in detail.

did not treat the "trivial" case of $4f^2$, but this was analyzed by Beatham et al. using configuration interaction within a *j*−*j* basis.[58] In Figure 6, the intensities and energies of the final state components from Gerken are represented by bars below the experimental spectra.

3.2.1. $BiVO_4$ and $Bi_{0.5}La_{0.5}VO_4$. The valence region spectrum of $BiVO_4$ provides the starting point for discussion of valence region spectra of $Bi_{0.5}La_{0.5}VO_4$ and the other lanthanide-doped materials. In agreement with previous work, two main spectral features may be identified: the O 2p valence band and a peak associated with Bi 6s states at higher binding energy.[29] As in Bi_2O_3,[26] the relatively deep Bi 6s states hybridize with O 2p states to give antibonding states at the top of the main valence band, and these further hybridize with nominally empty Bi 6p states to give the directional lone pair states responsible for the low symmetry coordination environment found for the Bi(III)

DOI: 10.1021/acs.jpcc.8b10573
J. Phys. Chem. C 2019, 123, 8484−8499

Table 1. One-Electron Ionization Cross-Sections (Mb) for Orbitals Involved in the Valence Bands of $Bi_{0.5}Ln_{0.5}VO_4$ Compounds

Bi 6s	Ce 4f	Lu 4f	V 3d	O 2s
6.5×10^{-4}	1.1×10^{-3}	6.9×10^{-3}	2.0×10^{-4}	9.5×10^{-3}
Bi 6p	Ce 5d[aI]	Lu 5d	V 4s	O 2p
1.4×10^{-3}	7.9×10^{-4}	9.7×10^{-4}	2.1×10^{-4}	6.0×10^{-5}
	Ce 6s		Lu 6s	
	1.6×10^{-4}		2.3×10^{-4}	

[aI]nterpolated from values for La and Lu.

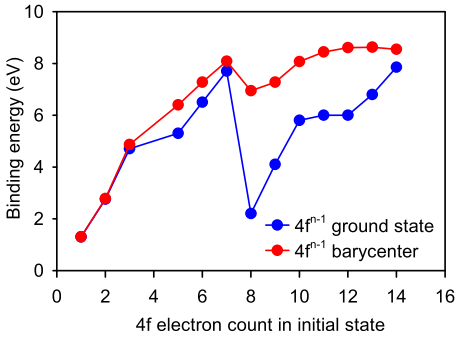

Figure 7. Variation in binding energies corresponding to the ground $4f^{n-1}$ final state and the barycentre of the $4f^{n-1}$ final states in X-ray photoemission spectra of $Bi_{0.5}Ln_{0.5}VO_4$ (Ln = Ce–Lu, excluding Pm) as a function of 4f electron count in the initial state.

ions in monoclinic $BiVO_4$.[28,30] The O 2p valence band spectrum for $Bi_{0.5}La_{0.5}VO_4$ is similar to that of the parent compound, although the overall bandwidth is a little smaller and shoulders to high and low binding energy of the central peak are less pronounced. However, the most pronounced difference lies in a reduction in the intensity of the Bi 6s peak relative to that of the O 2p valence band, as is to be expected from the change in stoichiometry. Note that both spectra contain weak in-gap structure just below the Fermi energy arising from occupied V 3d states associated with oxygen deficiency.

3.2.2. $Bi_{0.5}Ce_{0.5}VO_4$. A single sharp peak is observed above the main valence band of $Bi_{0.5}La_{0.5}VO_4$. As discussed previously, this must arise from the ionization of a single 4f electron characteristic of the $^2F_{5/2}$ states of Ce(III) to give a $^1S_0$ final state.[48] The observation of this peak is thus a diagnostic of Ce(III) + V(V) valence states: a much weaker 3d peak would be found for a Ce(IV) + V(IV) valence state configuration, owing to the lower ionization cross-section for V 3d as compared to Ce 4f. Core level spectroscopy confirms this assignment (see below).

3.2.3. $Bi_{0.5}Pr_{0.5}VO_4$. The valence band spectrum contains a well-defined shoulder overlapping the top of the O 2p valence band, similar to that found in the spectrum of Pr_2O_3.[59] In the L–S limit, the $^3H_4$ ground state of the $4f^2$ configuration gives rise to $^2F_{5/2}$ and $^2F_{7/2}$ final states, with an intensity ratio 1.714/0.286. In the j–j limit, only the $^2F_{5/2}$ state is reached, whereas in the intermediate coupling, the ratio lies between these two limits, with a value of 1.857/0.143.[58] The obvious shoulder is assigned to the $^2F_{5/2}$ final state, and the much weaker $^2F_{7/2}$ component must, therefore, be presumed to overlap the O 2p valence band. The significantly greater intensity of the 4f peak as compared to the Ce compound argues against the unlikely possibility that $Bi_{0.5}Pr_{0.5}VO_4$ contains $4f^1$ Pr(IV), a conclusion again supported by core level spectra (see below).

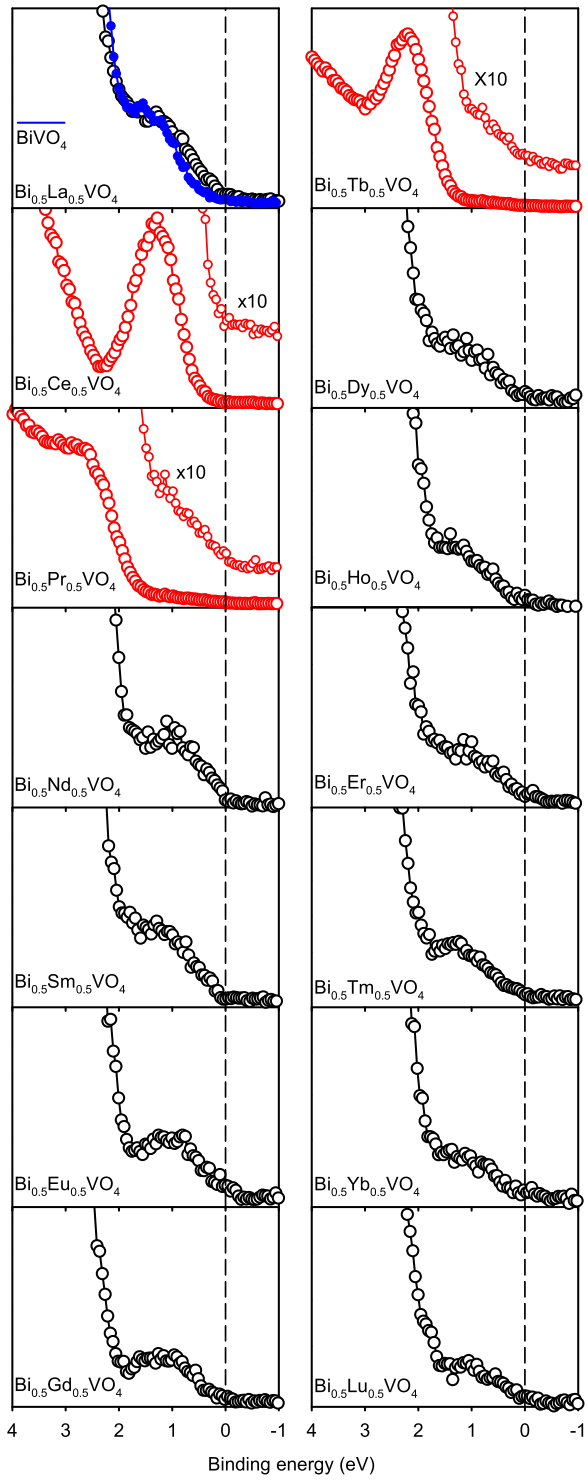

Figure 8. Onsets in valence band X-ray photoemission spectra of $Bi_{0.5}Ln_{0.5}VO_4$ (Ln = lanthanide, excluding Pm) solid solutions showing a weak structure in the bandgap above the main O 2p valence band edge. Binding energies are given relative to the Fermi energy. Spectra highlighted in red correspond to the Ln = Ce, Pr, and Tb, where the main onset of photoemission intensity is associated with Ln 4f states.

3.2.4. $Bi_{0.5}Nd_{0.5}VO_4$. The $4f^3$ configuration of Nd(III) gives a ground term $^4I_{9/2}$ in the L–S limit, with small contributions

DOI: 10.1021/acs.jpcc.8b10573
J. Phys. Chem. C 2019, 123, 8484–8499

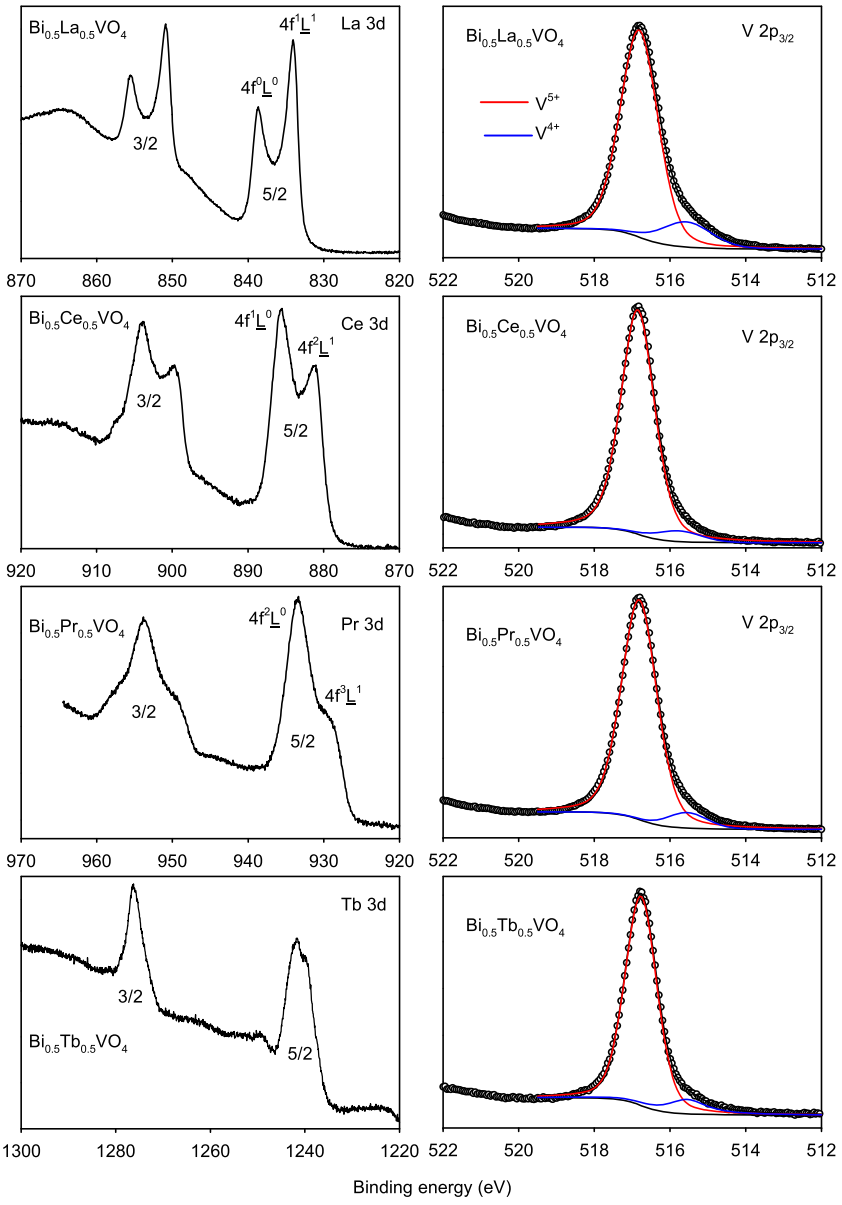

Figure 9. Ln 3d and V $2p_{3/2}$ core level photoelectron spectra of $Bi_{0.5}La_{0.5}VO_4$, $Bi_{0.5}Ce_{0.5}VO_4$, $Bi_{0.5}Pr_{0.5}VO_4$, and $Bi_{0.5}Tb_{0.5}VO_4$. The V $2p_{3/2}$ core lines have been fitted to two components corresponding to majority V(V) in red and (at lower binding energy in blue) V(IV) associated with oxygen vacancies.

Table 2. Details of V $2p_{3/2}$ Core Level XPS for $Bi_{0.5}La_{0.5}VO_4$, $Bi_{0.5}Ce_{0.5}VO_4$, $Bi_{0.5}Pr_{0.5}VO_4$, and $Bi_{0.5}Tb_{0.5}VO_4$

	$Bi_{0.5}La_{0.5}VO_4$	$Bi_{0.5}Ce_{0.5}VO_4$	$Bi_{0.5}Pr_{0.5}VO_4$	$Bi_{0.5}Tb_{0.5}VO_4$
		V(V) $2p_{3/2}$		
binding energy (eV)	516.82	516.85	516.81	516.77
FWHM (eV)	1.18	1.05	1.11	1.00
relative intensity	0.87	0.95	0.93	0.90
		V(IV) $2p_{3/2}$		
binding energy (eV)	515.57	515.78	515.54	515.55
FWHM (eV)	1.56	1.40	1.24	1.27
relative intensity	0.13	0.05	0.07	0.10

from two $^2H_{9/2}$ states in the intermediate coupling. The final state structure is dominated by $^3H_4$ and $^3F_2$ final states, with a separation calculated to be 0.61 eV. However, the 4f structure shows very strong overlap with the O 2p valence band, and the individual components are not easily identified in the spectrum.

3.2.5. $Bi_{0.5}Sm_{0.5}VO_4$. Sm(III) has a $4f^5$ valence electron configuration, giving a $^6H_{5/2}$ ground state, weakly mixed with four $^4G_{5/2}$ states in the intermediate coupling. Ionization yields principally $^5I_{6,5,4}$, $^5G_{4,3,2}$, $^5F_{3,2,1}$, and $^5D_{2,1,0}$ final states, with weak ^3H and ^3D states arising in the intermediate coupling. Yet again for the most part, the 4f structure overlaps the O 2p valence band, although shoulders associated with the 4f ionizations are more pronounced than for the Nd compound.

3.2.6. $Bi_{0.5}Eu_{0.5}VO_4$. The spectrum of $4f^6$ Eu(III) is simpler than that of the Sm compound. The nominally nonmagnetic $^7F_0$ ground state mixes with two $^5D_0$ states in the intermediate coupling. The final state spectrum is dominated by $^6H_{7/2,5/2}$, $^6F_{7/2,5/2}$, and $^6P_{7/2,5/2}$, along with weak $^4F_{5/2}$ and $^4P_{5/2}$ in the

DOI: 10.1021/acs.jpcc.8b10573
J. Phys. Chem. C 2019, 123, 8484−8499

Table 3. Binding Energies (in eV) and Relative Peak Heights (in Parenthesis) in Ln 3d Core XPS of $Bi_{0.5}La_{0.5}VO_4$, $Bi_{0.5}Ce_{0.5}VO_4$, $Bi_{0.5}Pr_{0.5}VO_4$, and $Bi_{0.5}Tb_{0.5}VO_4$[a,b]

		$Bi_{0.5}La_{0.5}VO_4$	$Bi_{0.5}Ce_{0.5}VO_4$	$Bi_{0.5}Pr_{0.5}VO_4$	$Bi_{0.5}Tb_{0.5}VO_4$
Ln $3d_{5/2}$	screened	834.0 (3.7)	881.1 (2.7)	929.8* (1.8)	1240.0* (2.6)
	unscreened	838.7 (2.3)	885.7 (3.3)	933.4 (4.2)	1241.9 (3.0)
					1249.2 (0.4)
Ln $3d_{3/2}$	screened	851.1 (2.6)	899.7 (1.7)	950.4* (1.1)	1272.8* (0.6)
	unscreened	855.5 (1.4)	904.0 (2.2)	953.9 (2.5)	1276.3 (2.2)
			907.8* (0.4)	958.0* (0.6)	1279.2* (0.6)

[a]The peak heights add to 6 for the components of Ln $3d_{5/2}$. In the case of the Tb compound, final state multiplet coupling dominates over the final state screening, and the classification of peaks in terms of screened and unscreened final states breaks down. For this reason, peak positions are given in italics and cannot be linked with the assignments in the first column as for the La, Ce, and Pr compounds. [b]* denotes a shoulder.

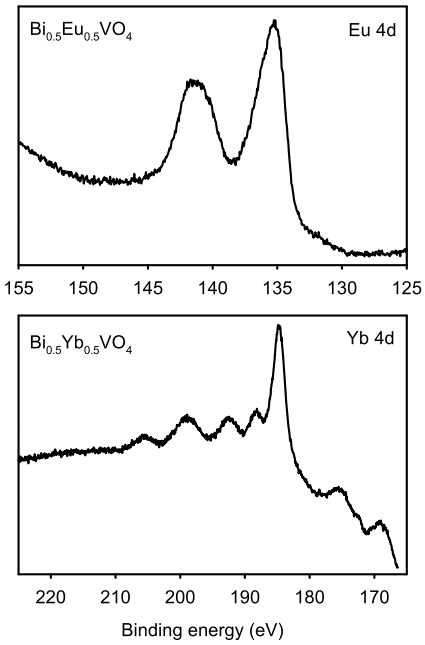

Figure 10. Ln 4d core level photoelectron spectra of $Bi_{0.5}Eu_{0.5}VO_4$ and $Bi_{0.5}Yb_{0.5}VO_4$.

intermediate coupling. The components of ^6H sit mainly on top of the O 2p valence band and those of ^6P are on top of the Bi 6s peak, whereas ^6F appears as a distinct shoulder on the high binding energy side of the valence band. The spectrum differs markedly from that of $4f^7$ Gd(III), thus establishing the presence of Eu(III) rather than Eu(II).

3.2.7. $Bi_{0.5}Gd_{0.5}VO_4$. The $^8S_{7/2}$ state (with weak mixing with $^6P_{7/2}$ and $^6D_{7/2}$ in the intermediate coupling) associated with the $4f^7$ configuration of Gd(III) gives rise to ^7F final states, with J values between 0 and 6, $^7F_0$ appearing at lowest binding energy. The intensities of these components increase monotonically from $J = 0$ to 6, with an overall energy spread calculated to be 0.63 eV. Thus, all of the components are contained within a single broad and asymmetric peak, whose maximum is at about 8 eV binding energy. This peak is distinct from the O 2p valence band.

3.2.8. $Bi_{0.5}Tb_{0.5}VO_4$. We note first that the spectrum of $Bi_{0.5}Tb_{0.5}VO_4$ differs markedly from that of $Bi_{0.5}Gd_{0.5}VO_4$, thus establishing the $4f^8$ configuration of Tb(III), rather than $4f^7$ for Tb(IV). The ground term for the $4f^8$ configuration is $^7F_6$, mixed with $J = 6$ components of three ^5G and one ^5H states in the intermediate coupling. Ionization from $4f^8$ is the first example where states of different spin multiplicities may be reached in the photoemission process in the $L-S$ limit. Above the O 2p valence band at lowest binding energy, a distinct peak associated with $^8S_{7/2}$ arises from ionization of the single minority spin electron. At higher binding energy and below the O 2p valence band, a complex band profile with two obvious maxima arises mainly from $^6I_{17/2,15/2,13/2,11/2}$; $^6G_{13/2,11/2,9/2,7/2}$; and $^6H_{15/2,13/2,11/2}$ final states, with weaker contributions from ^6F, ^6D, and ^6P sextuplets, and quartet states ^4L, ^4I and ^4H emerging as a consequence of the quintet contribution to the initial state.

3.2.9. $Bi_{0.5}Dy_{0.5}VO_4$. The $^6H_{15/2}$ ground term of the $4f^9$ configuration is mixed with two $^4I_{15/2}$ and a $^4K_{15/2}$ states in the intermediate coupling. The final state spectrum has 31 components listed by Gerken, dominated by ^7F spin septets and quintuplets ^5D, ^5F, ^5G, ^5H, ^5I, ^5K, and ^5L, with weaker triplets arising from the quartet contributions in the initial state. The lowest energy states are $^7F_{6,5,4}$, which appear as a relatively sharp feature at the top of the valence band at around 4 eV binding energy. This is to 2 eV higher binding energy compared with the minority spin peak of the Tb compound. A second distinct peak at just under 10 eV binding energy dominated by ^5K. The structure in between these two features contains contributions from ^5L, ^5I, and ^5G.

3.2.10. $Bi_{0.5}Ho_{0.5}VO_4$. The $4f^{10}$ configuration of Ho(III) gives a $^5I_8$ ground state, mixed with two $^3K_8$ and a $^3L_8$ state. Ionization yields sextets $^6H_{15/2,13/2,11/2,9/2}$ and $^6F_{11/2,9/2}$ and quartets ^4M, ^4L, ^4K, ^4I, ^4H, and ^4G, with 32 states tabulated by Gerken. The experimental spectrum reveals little of this complexity and is dominated by two 4f peaks at binding energies of about 6 and 9 eV. The first peak derives mainly from the sextets and the sharper second peak from the quartets.

3.2.11. $Bi_{0.5}Er_{0.5}VO_4$. The $^4I_{15/2}$ ground state of $4f^{11}$ Er(III) mixes with ^2K and ^2L states with $J = 15/2$. As with Tb, Dy, and Ho, final states with different spin multiplicities are found with both quintets ^5I, ^5G, and ^5F and triplets ^3M, ^3L, ^3K, ^3I, ^3H, ^3G, and ^3F. The experimental spectrum is quite similar to that for the Ho compound with a two-peak structure. The dominant contributions to the peak at low binding energy are from ^5I and ^5G multiplets, whereas the intensity in the higher binding energy peak is mainly from ^3M and ^3L states.

3.2.12. $Bi_{0.5}Tm_{0.5}VO_4$. The $^3H_6$ ground state of $4f^{12}$ Tm(III) mixes with $^1I_6$ in the intermediate coupling. Gerken lists 28 final state peaks for this lanthanide, extending across an energy range of over 12 eV. The most intense is $^4I_{15/2}$, which sits almost exactly on the top of the O 2p valence band at just under 6 eV binding energy, with $J = 13/2$ and $11/2$ components at higher binding energy. A distinct peak at about 11.5 eV binding energy is dominated by $^2L_{17/2}$. A second distinct peak below the main valence band with a binding

DOI: 10.1021/acs.jpcc.8b10573
J. Phys. Chem. C 2019, 123, 8484−8499

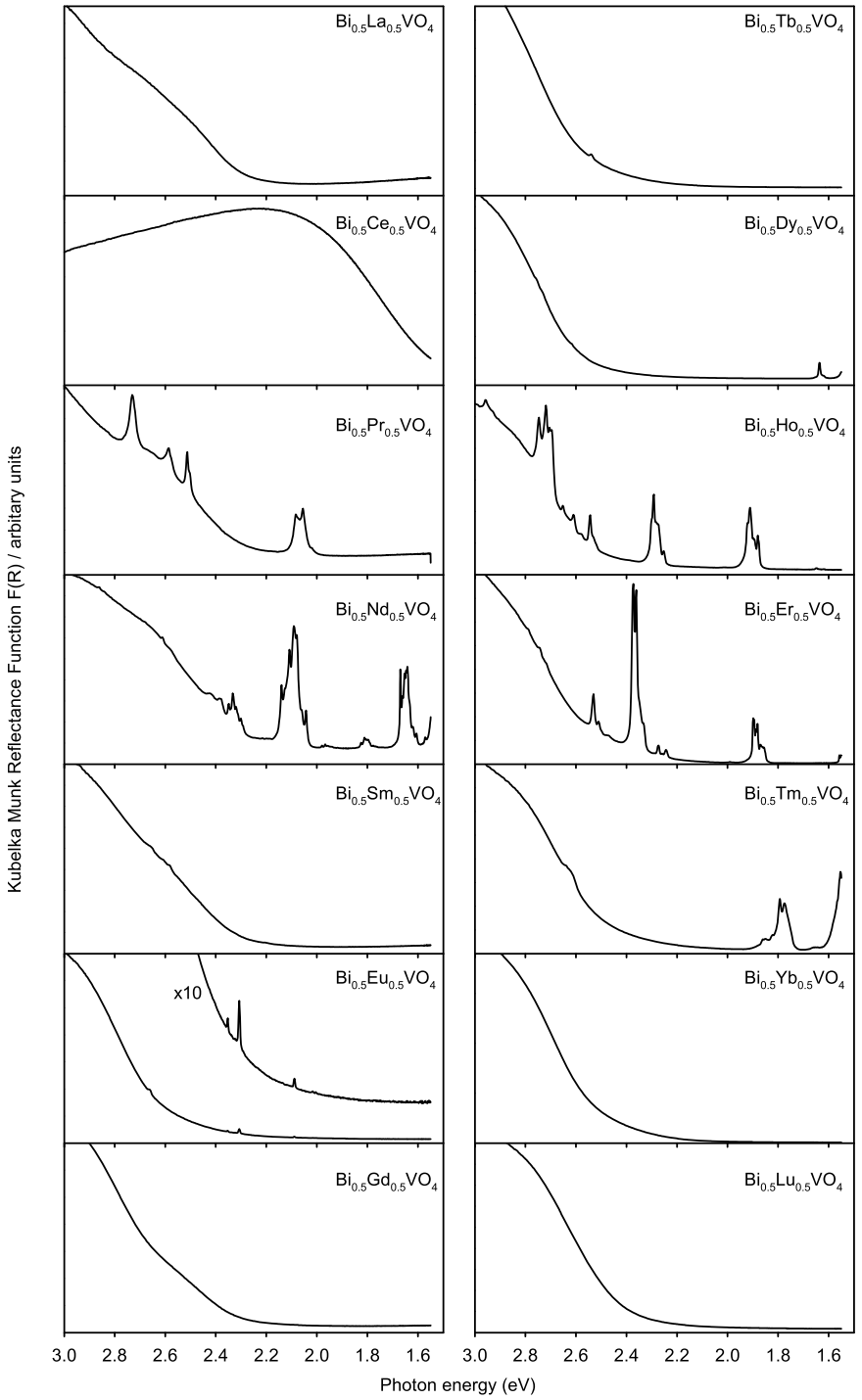

Figure 11. Diffuse reflectance spectra of $Bi_{0.5}Ln_{0.5}VO_4$ (Ln = lanthanide, excluding Pm) ceramics, presented as the Kubelka–Munk reflectance function $F(R)$ versus photon energy.

energy of about 9.5 eV contains major contributions from $^2K_{15/2}$, $^2H_{11/2}$, and $^4G_{11/2,9/2}$.

3.2.13. $Bi_{0.5}Yb_{0.5}VO_4$. The $4f^{13}$ configuration of Yb(III) gives a simple $^2F_{7/2}$ ground state. Ionization yields both triplet ($^3H_{6,5,4}$; $^3F_{4,3,2}$; and $^3P_{2,1,0}$) and singlet ($^1I_6$, $^1G_4$, $^1D_2$, and $^1S_0$, the last being very weak indeed) states. The different components of ^3H and ^3F overlap to give a dominant double-peaked structure centered at about 7 eV binding energy, whereas ^1I and ^1D are found in a separate peak beyond 10 eV. The ^3P states overlap the strong singlets, whereas the ^1G peak overlaps the strong triplets. The complexity of the final state structure associated with 4f ionization contrasts with the simple spin–orbit doublet found for $Bi_{0.5}Lu_{0.5}VO_4$ (see below) and in mixed valency compounds such as $Yb_{14}MnSb_{11}$, which contains Yb(II).[60] This establishes that $Bi_{0.5}Yb_{0.5}VO_4$ does not contain $4f^{14}$ Yb(II).

3.2.14. $Bi_{0.5}Lu_{0.5}VO_4$. The $4f^{14}$ configuration of Lu(III) gives a $^1S_0$ ground state, ionization of which yields a simple $^2F_{7/2}$ + $^2F_{5/2}$ doublet. This appears on the high binding energy side of the O 2p valence band, which now appears as a relatively weak feature extending up to 2 eV.

DOI: 10.1021/acs.jpcc.8b10573
J. Phys. Chem. C 2019, 123, 8484–8499

Table 4. Bandgaps in $Bi_{0.5}Ln_{0.5}VO_4$ Compounds Derived from Diffuse Reflectance Spectra

Ln	bandgap (eV)	Ln	bandgap (eV)
La	2.43	Tb	2.62
Ce	1.69	Dy	2.66
Pr	2.41	Ho[a]	2.64
Nd	2.42	Er	2.63
Sm	2.50	Tm	2.61
Eu	2.64	Yb	2.60
Gd	2.60	Lu	2.55

[a]Overlap of 4f → 4f transitions with the band edge precludes analysis and the value is derived from interpolation between Dy and Er solid solutions.

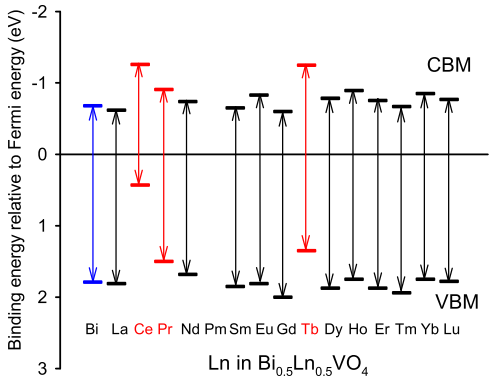

Figure 12. Positions of valence and conduction band edges relative to the Fermi energy derived from photoemission and diffuse reflectance optical spectra of monoclinic $BiVO_4$ and $Bi_{1-x}Ln_xVO_4$ solid solutions. Compounds, where Ln 4f states are observed above the main valence band edge in photoemission spectra, are highlighted in red.

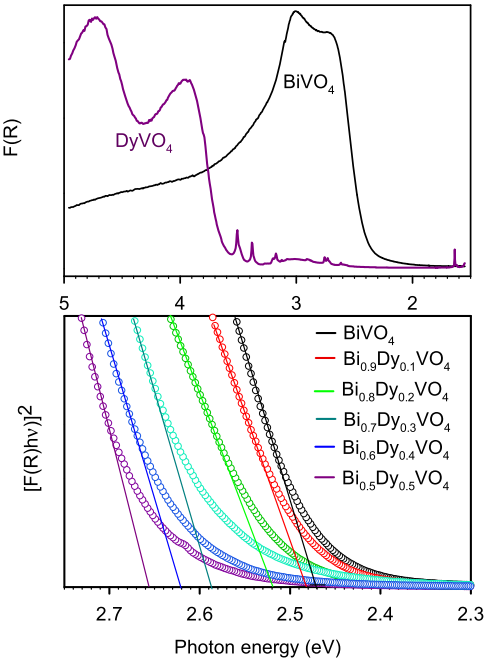

Figure 13. Diffuse reflectance spectra of $DyVO_4$ and $Bi_{0.5}Dy_{0.5}VO_4$ ceramics, presented as the Kubelka–Munk reflectance function $F(R)$ versus photon energy. The lower panel shows plots of $(h\nu F(R))^2$ versus photon energy $h\nu$ for $Bi_{1-x}Dy_xVO_4$ solid solutions with $0 < x < 0.5$ used to derive values of the bandgaps.

Table 5. Bandgaps for $Bi_{1-x}Dy_xVO_4$ Compounds Derived from Diffuse Reflectance Spectra

x	bandgap (eV)	x	bandgap (eV)
0.00	2.47	0.30	2.59
0.05	2.47	0.40	2.62
0.10	2.48	0.50	2.66
0.20	2.52	1.00	3.72

3.2.15. Summary of Overall Trends. Despite the complexity of the spectra, it is evident in comparing the series of compounds between Ce and Gd that there is a progressive shift to high binding energy in both the lowest 4f binding energy and the barycentre for 4f electron final states. These trends are summarized in Figure 7 (numerical values are given in Table S3 in the Supporting Information). A new low binding energy 4f peak ($^8S_{7/2}$) appears for $Bi_{0.5}Tb_{0.5}VO_4$, associated with the ionization of the minority spin electron within the $4f^8$ configuration. The spectra for the series between Tb and Yb reveal a progressive stabilization of states with the higher of the two dominant spin multiplicities, associated with the ionization of the minority spin electrons, repeating the trend seen in the first half of the lanthanide series (see Figure 7). In general, there is a pleasing correspondence between the structure in the experimental spectra and the calculations of Gerken.[57] However, it is noticeable in several cases (particularly for $Bi_{0.5}Tb_{0.5}VO_4$) that the overall energy spread in the 4f final states is somewhat bigger in the experimental spectra than in the calculations. Finally, we note that the current spectra are consistent with valence region spectra for a more restricted range of lanthanide tantalates $LnTaO_4$ (Ln = La, Ce, Pr, Nd, Sm).[61]

3.3. Photoemission Onsets. Expansions of the onset region in photoemission spectra are shown in Figure 8, with binding energies referenced to the Fermi energy. In most cases, the onset of strong structure in the photoemission spectra is associated with O 2p states (hybridized with Bi 6s states as discussed earlier). However, for the Ce, Pr, and Tb solid solutions, the main onset involves Ln 4f states. Above the main band edge, the weaker structure in the bandgap is observed for all of the compounds aside from $Bi_{0.5}Ce_{0.5}VO_4$, typically reaching maximum intensity just above 1 eV binding energy. This structure is assigned to occupied V(IV) $3d^1$ states arising from oxygen deficiency: the peak maximum binding energy is similar to that in V(IV)-doped TiO_2.[62] The localized V 3d electrons will produce a polaronic elongation of local V–O bond lengths, and the peak maximum in photoemission is associated with a vertical ionization process in which the V–O bondlength is unchanged and a vibrationally excited final state is reached. Moreover, the Fermi energy appears to be pinned by the adiabatic V 3d ionization energy (that is the energy difference between the initial state and the vibrational ground state in the electronic final state).[62,63]

3.4. Core Level Photoelectron Spectra. Core level photoelectron spectra were used to probe the lanthanide and vanadium valence states in those compounds where the lanthanide could possibly adopt a higher Ln(IV) oxidation state, i.e., in the compounds involving Ce, Pr, or Tb as the dopant, where in principle the compounds could be formulated as $Bi(III)_{0.5}Ln(IV)_{0.5}V(IV)_{0.5}V(V)_{0.5}O_4$ rather than $Bi(III)_{0.5}Ln(III)_{0.5}V(V)O_4$.[48] Ln 3d and V $2p_{3/2}$ spectra for $Bi_{0.5}Ce_{0.5}VO_4$, $Bi_{0.5}Pr_{0.5}VO_4$, and $Bi_{0.5}Tb_{0.5}VO_4$ are shown in

DOI: 10.1021/acs.jpcc.8b10573
J. Phys. Chem. C 2019, 123, 8484–8499

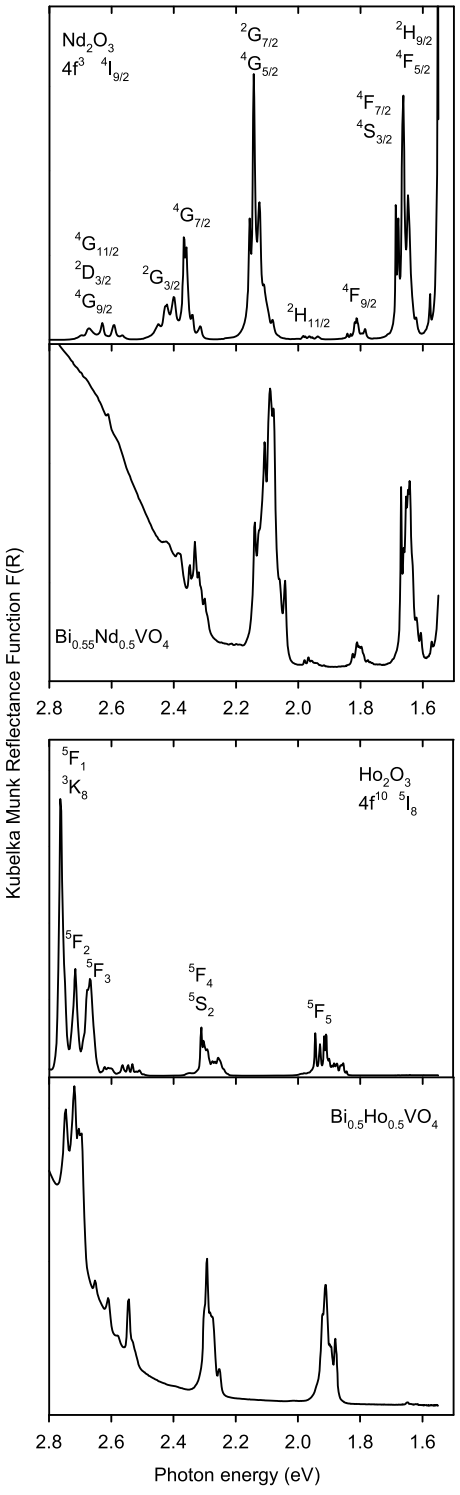

Figure 14. Comparison of diffuse reflectance spectra of $Bi_{0.5}Nd_{0.5}VO_4$ and $Bi_{0.5}Ho_{0.5}VO_4$ with those of Nd_2O_3 and Ho_2O_3 in the region of 4f excitations.

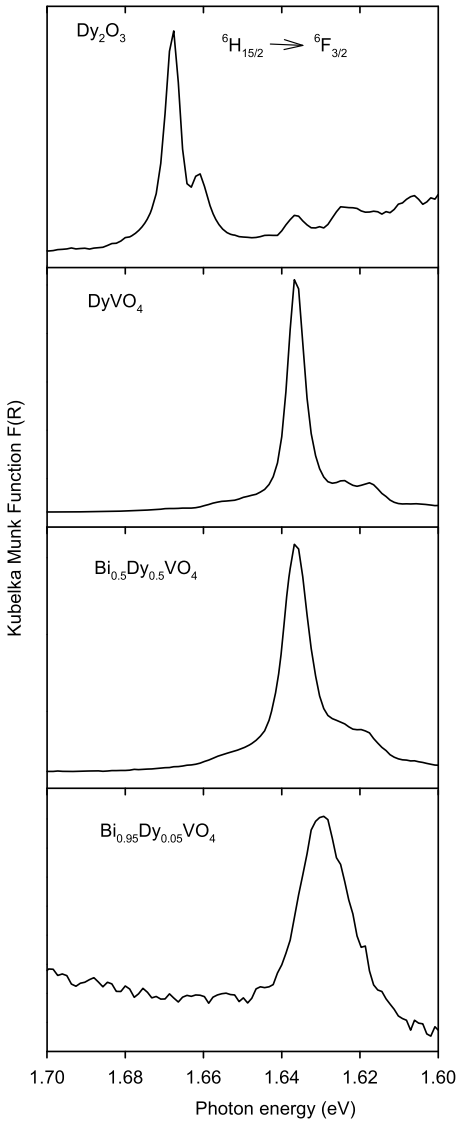

Figure 15. Comparison of the $^6H_{15/2} \rightarrow {}^6F_{5/2}$ excitations in diffuse reflectance spectra of Dy_2O_3, $DyVO_4$, $Bi_{0.5}Dy_{0.5}VO_4$, and $Bi_{0.05}Dy_{0.05}VO_4$ showing shift in the excitation to lower energy in this series of compounds.

Figure 9, along with reference spectra for $Bi_{0.5}La_{0.5}VO_4$ where there is no ambiguity about valence states.

The results of curve fitting the V $2p_{3/2}$ spectral profile are summarized in Table 2. In all cases, spectra are dominated by a component with a binding energy of 516.8 ± 0.1 eV for the V $2p_{3/2}$ level characteristic of V(V).[64] A weaker peak appears at a lower binding energy of 515.6 ± 0.2 eV, corresponding to a chemical shift of just over 1 eV. The second component arises from the oxygen deficiency discussed earlier, leading to occupied V 3d states. The V(IV) structure is weakest for $Bi_{0.5}Ce_{0.5}VO_4$, where V 3d structure is not evident in valence region photoemission spectra (although it may be masked to some extents by Ce 4f states).

The Ln 3d spectra are more complicated. In the spectrum of $Bi_{0.5}La_{0.5}VO_4$, the $3d_{5/2}$ and $3d_{3/2}$ peaks are each split into two components. The origins of this splitting have been discussed extensively in the published literature in terms of configuration mixing in the initial state and final state screenings. In outline, the weaker high binding energy component arises from a final state corresponding to a $4f^0$ valence configuration, whereas the stronger component at lower binding energy is associated with $4f^1$ in the final state, with a hole on the ligand (oxygen) atoms. The latter $4f^1$ configuration is present to some extents in the initial state due to La 4f−O 2p covalency, but the intensity is enhanced by final state charge-transfer screening from oxygen into the 4f level.[65−67] The Ln 3d spectrum of $Bi_{0.5}Ce_{0.5}VO_4$ is similar to that of the La compound, although the relative

DOI: 10.1021/acs.jpcc.8b10573
J. Phys. Chem. C 2019, 123, 8484−8499

intensity of the low binding energy components is weaker and the peaks are less well resolved. In addition, a distinct shoulder appears on the high binding energy side of the $3d_{3/2}$ component. The spectrum is similar to that of Ce_2O_3[66−68] but is very different to that found for CeO_2.[65,68−72] In the latter material, a very complicated spectral profile arises from a superposition of three different final state configurations: $4f^0\underline{L}^0$, $4f^1\underline{L}^1$, $4f^2\underline{L}^2$, where $\underline{L}$ signifies a hole on a ligand (oxygen) atom. The ground state is a mixture of $4f^0\underline{L}^0$ and $4f^1\underline{L}^1$, and the final state screening allows the appearance of $4f^2\underline{L}^2$. The two-peaked structure for $Bi_{0.5}Ce_{0.5}VO_4$ arises from $4f^1\underline{L}^0$ and $4f^2\underline{L}^1$ final states, the absence of peaks associated with $4f^0$ rules out the incorporation of Ce(IV) in the ternary material. Similar arguments pertain for $Bi_{0.5}Pr_{0.5}VO_4$ where the two-component structure arises from $4f^2\underline{L}^0$ and $4f^3\underline{L}^1$ final states. No peaks at higher binding energy associated with a $4f^1\underline{L}^0$ configuration that would be diagnostic of Pr(IV) as found, in contrast to Pr(IV) compounds such as PrO_2[73,74] and $BaPrO_3$.[75,76] The screened final state peaks are much weaker than for the La and Ce compounds, and the broadening and extra structure on the $3d_{3/2}$ peak are more pronounced. This is due to the less pronounced Ln 4f−O 2p mixing in the initial state and the exchange and orbital coupling of the core hole with the $4f^2$ and $4f^3$ open shells.[77] Finally, for $Bi_{0.5}Tb_{0.5}VO_4$, the 3d spectrum is similar to that found for the Tb(III) compound $TbPO_4$.[78] The $3d_{5/2}$ component shows an incipient splitting due to the coupling of the core hole to the $4f^8$ open shell, hinting at two main components. Much more pronounced splitting is found for Tb(IV) compounds such as TbO_2,[67,73] and hence core level XPS is again diagnostic of an Ln(III) valence state.

Although the Ln 3d peaks in Figure 9 are labeled on the basis of dominant screened and unscreened final state configurations contributing to the peak intensities, the spectra have a much greater underlying complexity associated with the plethora of final states allowed when a Ln 3d core hole couples with an open shell $4f^n$ final state configuration, as discussed above and detailed by Kotani et al.[67,77] For this reason, it is not possible to perform physically meaningful curve fits to the peak profiles with a small and manageable number of components. However, for completeness, we list in Table 3 the main identifiable binding energies (of peaks and shoulders) as well peak (or shoulder) heights above a linear baseline.

Ln core level spectra were also measured for $Bi_{0.5}Eu_{0.5}VO_4$ and $Bi_{0.5}Yb_{0.5}VO_4$ where Ln(II) valence states are allowed in principle, although changes in the vanadium valence beyond V(V) could not compensate for the lower charge on the lanthanide, and oxygen deficiency would be required. The 4d spectrum of $Bi_{0.5}Yb_{0.5}VO_4$ shown in Figure 10 has the same structure as that reported previously for Yb_2O_3[65,77,79−81] and is much more complicated than the simple spin−orbit doublet anticipated when the valence configuration is $4f^{14}$ (as in Lu_2O_3[75]) due to the final state orbital and exchange coupling with the open 4f shell. Thus, core XPS confirms the conclusion from the 4f spectra that $Bi_{0.5}Yb_{0.5}VO_4$ contains $4f^{13}$ Yb(III) and not $4f^{14}$ Yb(II). Similarly, the 4d spectrum of $Bi_{0.5}Eu_{0.5}VO_4$ is in agreement with that published previously for Eu_2O_3,[81] thus establishing the presence of $4f^6$ Eu(III) and not $4f^7$ Eu(III).

3.5. Optical Spectra. Diffuse reflectance spectra of the complete series of quaternary bismuth lanthanide vanadates are shown in Figure 11, where data in the energy range between 1.55 and 3.00 eV are plotted with the Kubelka−Munk reflectance function $F(R)$ against photon energy $h\nu$. Bandgaps were derived from plots of $[F(R)h\nu]^2$ against $h\nu$ (Supporting Information Figure S5) and are given in Table 4. With the exception of the Ce compound, all of the quaternary vanadates $Bi_{0.5}Ln_{0.5}VO_4$ show a broad but pronounced increase in absorbance above 2.4 eV associated with transitions between the valence and conduction bands. More specifically, the bandgaps of the early lanthanide solid solutions with Ln = La, Pr, Nd (bandgaps 2.43, 2.41, 2.42 eV) are a little smaller than for monoclinic $BiVO_4$ (our estimate of the bandgap is 2.46 eV, see below). For the Sm compound, the bandgap is estimated as 2.50 eV, whereas between Eu and Yb bandgaps are 2.6 eV or greater, reaching a maximum of 2.66 eV for the Dy compound. In the case of the Ce compound, the absorption edge is at much lower energy, and the bandgap is estimated as 1.69 eV. The small value for $Bi_{0.5}Ce_{0.5}VO_4$ presumably arises from excitations from the 4f state above the main O 2p valence band into the conduction band, the lower part of which is dominated by mixed Bi 6p and V 3d character.[48] The Ce 5d contribution to the conduction band is at higher energy, so it is not correct to think of the lowest energy transitions as Ce 4f → Ce 5d.

In addition to the broad interband structure, the spectra of the Pr, Nd, Eu, Dy, Ho, Er, and Tm compounds contain sharp visible region excitations associated with 4f → 4f transitions. These may all be assigned by reference to energy level diagrams reproduced in the textbook by Henderson and Imbusch.[82] In the case of the Pr, Nd, Ho, and Er compounds, some of the 4f structure are superimposed on the band edge, and it becomes difficult to derive a bandgap from the usual linear extrapolation, especially for $Bi_{0.5}Ho_{0.5}VO_4$.

The bandgap values discussed above may be combined with the measurements of the positions of valence band onsets (Section 3.3) to show the positions of the valence and conduction band edges relative to the Fermi level, see Figure 12. With the exception of the Ce, Pr, and Tb compounds, the Fermi level is seen to be positioned toward the top of the bulk bandgap, as expected for n-type materials where the Fermi level is defined by $3d^1$ V(IV) donor states. For $Bi_{0.5}Ce_{0.5}VO_4$, the Fermi level is closer to the valence band edge than the conduction band mimimum, pointing toward p-type behavior. This is understandable in simple chemical terms given that it is possible to envisage the introduction of holes into the Ce $4f^1$ band. The Fermi levels for $Bi_{0.5}Pr_{0.5}VO_4$ and $Bi_{0.5}Tb_{0.5}VO_4$ appear roughly in the middle of the gap, suggesting an interplay between n-type behavior (reduction of V(V) to V(IV)) and p-type behavior (oxidation of Pr(III) or Tb(III) to Pr(IV) and Tb(IV), respectively).

Spectra of $BiVO_4$ and $DyVO_4$ and intermediate solid solutions are compared in Figure 13. Given that the bandgap of $Bi_{0.5}Dy_{0.5}VO_4$ (2.66 eV) is bigger than that of $BiVO_4$ (2.47 eV), it is not surprising to find a progressive increase in the bandgap with Dy doping level in the quaternary solid solutions (Table 5) with intermediate composition, as shown in the lower panel of Figure 13. This demonstrates a potentially useful tunability, which presumably applies for the other later lanthanides as well.

Expansions of parts of the visible region 4f → 4f spectra for $Bi_{0.5}Nd_{0.5}VO_4$ and $Bi_{0.5}Ho_{0.5}VO_4$ are shown in Figure 14, along with spectra for the corresponding parent oxides Nd_2O_3 and Ho_2O_3. A more complete set of comparisons of 4f → 4f spectra for $Bi_{0.5}Ln_{0.5}VO_4$ and Ln_2O_3, including additional data for Ln = Pr, Sm, Eu, Dy, Er, Tm, is given as the Supporting Information (Figures S6 and S7). In outline, the spectra of the binary oxides show sharp bands at similar energies to those found for

DOI: 10.1021/acs.jpcc.8b10573
J. Phys. Chem. C 2019, 123, 8484−8499

the quaternary vanadates. However, in detail, the bandshapes do differ between the two. This is because although the spectra are dominated by intra-atomic repulsions and spin−orbit coupling, crystal field effects are not negligible, and the coordination environment in the sesquioxides is different to that in the zircon-type vanadates. In most cases, when comparing 4f → 4f spectra of the sesquioxides and the vanadates, small shifts to lower energy are apparent in the latter.

To explore this red shift effect in more detail, Figure 15 compares diffuse reflectance spectra of Dy_2O_3 with those of $DyVO_4$, $Bi_{0.5}Dy_{0.5}VO_4$, and $Bi_{0.95}Dy_{0.05}VO_4$ in the region of the $^6H_{15/2} \rightarrow {}^6F_{3/2}$ transition between 1.6 and 1.7 eV. The excitation energy is seen to decrease in this series of compounds. Quoted values of the bandgap for Dy_2O_3 range between 4.7 and 5.0 eV,[83] whereas as discussed above, the bandgap decreases from about 3.72 eV for $DyVO_4$, through 2.66 eV for $Bi_{0.5}Dy_{0.5}VO_4$, and 2.47 eV for $Bi_{0.95}Dy_{0.05}VO_4$. There is, thus, a direct inverse correlation between the bandgap of the host material and the 4f → 4f excitation energy. The decrease in bandgap may, in turn, be linked to an increase in the dielectric constant. From measurements of the refractive index as a function of wavelength reported by Medenbach et al.,[84] the dielectric constant of Dy_2O_3 may be estimated as 3.81 at 1.65 eV. For $BiVO_4$, a much larger value of about 9.0 was calculated by Yuan et al. based on density functional calculations within the generalized gradient approximation.[85] This accords with the idea that Bi^{3+} is highly polarizable. The Coulomb interelectronic repulsions, which play a large part in determining the energy 4f → 4f excitations, appear to be screened to some extents by the background dielectric constant within which the Ln^{3+} ions find themselves embedded. Expansions similar to that for $Bi_{0.5}Dy_{0.5}VO_4$ and Dy_2O_3 for the lanthanides Ln = Pr, Nd, Ho, and Tm are given as the Supporting Information (Figure S8), showing similar shifts to lower energy in the quaternary vanadates.

4. CONCLUDING REMARKS

The $Bi_{0.5}Ln_{0.5}VO_4$ quaternary vanadates form an isostructural series extending from La to Lu, and lattice parameters decrease in a monotonic fashion in traversing the lanthanide series. Analysis of both the 4f final state structure superimposed on the valence band and Ln 3d or 4d core level spectra confirms that in all cases the lanthanides are trivalent: the smooth variation in lattice parameters across the lanthanide series is consistent with this conclusion. Bandgaps for the later lanthanides are found to be slightly larger than for the monoclinic $BiVO_4$. The shift of the conduction band edge implied by these observations helps to explain why compounds such as tetragonal $Bi_{0.5}Dy_{0.5}VO_4$ can act as water splitting catalysts, the conduction band edge presumably being pushed sufficiently above its position in $BiVO_4$ to allow for the reduction of water by photoexcited electrons in the conduction band. Overall, there are many opportunities to tune the energies of both the interband and 4f → 4f transitions in these compounds, which could be exploited in future functional applications.

■ ASSOCIATED CONTENT

Supporting Information

The Supporting Information is available free of charge on the ACS Publications website at DOI: 10.1021/acs.jpcc.8b10573.

Complete set of powder diffraction patterns; lattice parameters; Rietveld profile refinements for $Bi_{0.5}Ce_{0.5}VO_4$ and $Bi_{0.5}Tm_{0.5}VO_4$; complete set of the valence band and shallow core level XPS data; binding energies of $4f^{n-1}$ ground states and $4f^{n-1}$ barycenters; plots of $[F(R)h\nu]^2$ versus photon energy $h\nu$; comparisons of diffuse reflectance spectra of $Bi_{0.5}Ln_{0.5}VO_4$ solid solutions with those of Ln_2O_3 for Ln = Pr, Nd, Eu, Sm, Dy, Ho, Er, Tm in the region of 4f excitations, including expanded scans for Pr, Nd, Ho, Tm (PDF)

■ AUTHOR INFORMATION

Corresponding Authors

*E-mail: F.E.Oropeza.Palacio@tue.nl (F.E.O.).
*E-mail: kelvinzhang@xmu.edu.cn (K.H.L.Z.).

ORCID

Freddy E. Oropeza: 0000-0001-7222-9603
Kelvin H. L. Zhang: 0000-0001-9352-6236
Anna Regoutz: 0000-0002-3747-3763

Notes

The authors declare no competing financial interest.

■ ACKNOWLEDGMENTS

K.H.L.Z. gratefully acknowledges the funding the Thousand Youth Talents Program at Xiamen University.

■ REFERENCES

(1) Fujishima, A.; Honda, K. Electrochemical photolysis of water at a semiconductor electrode. *Nature* **1972**, *238*, 37−38.
(2) Schrauzer, G. N.; Guth, T. D. Photolysis of water and photoreduction of nitrogen on titanium-dioxide. *J. Am. Chem. Soc.* **1977**, *99*, 7189−7193.
(3) Maeda, K. Photocatalytic water splitting using semiconductor particles: History and recent developments. *J. Photochem. Photobiol., C* **2011**, *12*, 237−268.
(4) Maeda, K.; Higashi, M.; Lu, D. L.; Abe, R.; Domen, K. Efficient nonsacrificial water splitting through two-step photoexcitation by visible light using a modified oxynitride as a hydrogen evolution photocatalyst. *J. Am. Chem. Soc.* **2010**, *132*, 5858−5868.
(5) Maeda, K. Z-scheme water splitting using two different semiconductor photocatalysts. *ACS Catal.* **2013**, *3*, 1486−1503.
(6) Li, R. G. Latest progress in hydrogen production from solar water splitting via photocatalysis, photoelectrochemical, and photovoltaic-photoelectrochemical solutions. *Chin. J. Catal.* **2017**, *38*, 5−12.
(7) Kudo, A.; Omori, K.; Kato, H. A novel aqueous process for preparation of crystal form-controlled and highly crystalline $BiVO_4$ powder from layered vanadates at room temperature and its photocatalytic and photophysical properties. *J. Am. Chem. Soc.* **1999**, *121*, 11459−11467.
(8) Tan, H. L.; Amal, R.; Ng, Y. H. Alternative strategies in improving the photocatalytic and photoelectrochemical activities of visible light-driven $BiVO_4$: a review. *J. Mater. Chem. A* **2017**, *5*, 16498−16521.
(9) Lamm, B.; Trzesniewski, B. J.; Doscher, H.; Smith, W. A.; Stefik, M. Emerging postsynthetic improvements of $BiVO_4$ photoanodes for solar water splitting. *ACS Energy Lett.* **2018**, *3*, 112−124.
(10) Li, P.; Chen, X. Y.; He, H. C.; Zhou, X.; Zhou, Y.; Zou, Z. G. Polyhedral 30-faceted $BiVO_4$ microcrystals predominantly enclosed by high-index planes promoting photocatalytic water-splitting activity. *Adv. Mater.* **2018**, *30*, No. 1703119.
(11) Pihosh, Y.; Turkevych, I.; Mawatari, K.; Uemura, J.; Kazoe, Y.; Kosar, S.; Makita, K.; Sugaya, T.; Matsui, T.; Fujita, D.; et al. Photocatalytic generation of hydrogen by core-shell $WO_3/BiVO_4$ nanorods with ultimate water splitting efficiency. *Sci. Rep.* **2015**, *5*, No. 11141.

DOI: 10.1021/acs.jpcc.8b10573
J. Phys. Chem. C 2019, 123, 8484−8499

(12) Zhang, L. M.; Ye, X. F.; Boloor, M.; Poletayev, A.; Melosh, N. A.; Chueh, W. C. Significantly enhanced photocurrent for water oxidation in monolithic Mo:$BiVO_4$/SnO_2/Si by thermally increasing the minority carrier diffusion length. *Energy Environ. Sci.* **2016**, *9*, 2044−2052.
(13) Li, Y.; Zhu, J.; Chu, H.; Wei, J. F.; Liu, F.; Lv, M.; Tang, J. W.; Zhang, B.; Yao, J. X.; Huo, Z. P.; Hu, L. H.; Dai, S. Y. $BiVO_4$ semiconductor sensitized solar cells. *Sci. China: Chem.* **2015**, *58*, 1489−1493.
(14) Liu, Z. K.; Yan, F. The application of bismuth-based oxides in organic-inorganic hybrid photovoltaic devices. *J. Am. Ceram. Soc.* **2012**, *95*, 1944−1948.
(15) Yang, Y. X.; Wang, J. R.; Zhao, J.; Nail, B. A.; Yuan, X.; Guo, Y. H.; Osterloh, F. E. Photochemical charge separation at particle interfaces: the n-$BiVO_4$-p-silicon system. *ACS Appl. Mater. Interfaces* **2015**, *7*, 5959−5964.
(16) Han, L. H.; Abdi, F. F.; van de Krol, R.; Liu, R.; Huang, Z. Q.; Lewerenz, H. J.; Dam, B.; Zeman, M.; Smets, A. H. M. Efficient water-splitting device based on a bismuth vanadate photoanode and thin-film silicon solar cells. *ChemSusChem* **2014**, *7*, 2832−2838.
(17) Ding, C. M.; Qin, W.; Wang, N.; Liu, G. J.; Wang, Z. L.; Yan, P. L.; Shi, J. Y.; Li, C. Solar-to-hydrogen efficiency exceeding 2.5% achieved for overall water splitting with an all earth-abundant dual-photoelectrode. *Phys. Chem. Chem. Phys.* **2014**, *16*, 15608−15614.
(18) Han, L. H.; Abdi, F. F.; Rodriguez, P. P.; Dam, B.; van de Krol, R.; Zeman, M.; Smets, A. H. M. Optimization of amorphous silicon double junction solar cells for an efficient photoelectrochemical water splitting device based on a bismuth vanadate photoanode. *Phys. Chem. Chem. Phys.* **2014**, *16*, 4220−4229.
(19) Han, L. H.; Abdi, F. F.; van de Krol, R.; Dam, B.; Zeman, M.; Smets, A. H. M. *Optical Modeling of an Efficient Water Splitting Device Based on Bismuth Vanadate Photoanode and Micromorph Silicon Solar Cells*, IEEE 40th Photovoltaic Specialist Conference, 2014; pp 3083−3086.
(20) Kosar, S.; Pihosh, Y.; Turkevych, I.; Mawatari, K.; Uemura, J.; Kazoe, Y.; Makita, K.; Sugaya, T.; Matsui, T.; Fujita, D.; et al. Tandem photovoltaic-photoelectrochemical GaAs/InGaAsP-WO_3/$BiVO_4$ device for solar hydrogen generation. *Jpn. J. Appl. Phys.* **2016**, *55*, No. 04ES01.
(21) Xiao, S.; Hu, C.; Lin, H.; Meng, X. Y.; Bai, Y.; Zhang, T.; Yang, Y. L.; Qu, Y. Q.; Yan, K. Y.; Xu, J. B.; et al. Integration of inverse nanocone array based bismuth vanadate photoanodes and bandgap-tunable perovskite solar cells for efficient self-powered solar water splitting. *J. Mater. Chem. A* **2017**, *5*, 19091−19097.
(22) Frost, R. L.; Henry, D. A.; Weier, M. L.; Martens, W. Raman spectroscopy of three polymorphs of $BiVO_4$: clinobisvanite, dreyerite and pucherite, with comparisons to three (VO_4)-bearing minerals: namibite, pottsite and schumacherite. *J. Raman Spectrosc.* **2006**, *37*, 722−732.
(23) Qurashi, M. M.; Barnes, W. H. The structure of pucherite, $BiVO_4$. *Am. Mineral.* **1953**, *38*, 489−500.
(24) Dreyer, G.; Tillmanns, E. Dreyerite - natural, tetragonal bismuth vanadate from hirschhorn-pfalz. *Neues Jahrb. Mineral., Monatsh.* **1981**, 151−154.
(25) Sleight, A. W.; Chen, H. Y.; Ferretti, A.; Cox, D. E. Crystal-growth and structure of $BiVO_4$. *Mater. Res. Bull.* **1979**, *14*, 1571−1581.
(26) Walsh, A.; Watson, G. W.; Payne, D. J.; Edgell, R. G.; Guo, J. H.; Glans, P. A.; Learmonth, T.; Smith, K. E. Electronic structure of the alpha and delta phases of Bi_2O_3: a combined *ab initio* and x-ray spectroscopy study. *Phys. Rev. B* **2006**, *73*, No. 235104.
(27) Payne, D. J.; Egdell, R. G.; Walsh, A.; Watson, G. W.; Guo, J.; Glans, P. A.; Learmonth, T.; Smith, K. E. Electronic origins of structural distortions in post-transition metal oxides: experimental and theoretical evidence for a revision of the lone pair model. *Phys. Rev. Lett.* **2006**, *96*, No. 157403.
(28) Walsh, A.; Payne, D. J.; Egdell, R. G.; Watson, G. W. Stereochemistry of post-transition metal oxides: revision of the classical lone pair model. *Chem. Soc. Rev.* **2011**, *40*, 4455−4463.
(29) Payne, D. J.; Robinson, M. D. M.; Egdell, R. G.; Walsh, A.; McNulty, J.; Smith, K. E.; Piper, L. F. J. The nature of electron lone pairs in $BiVO_4$. *Appl. Phys. Lett.* **2011**, *98*, No. 212110.
(30) Walsh, A.; Yan, Y.; Huda, M. N.; Al-Jassim, M. M.; Wei, S. H. Band edge electronic structure of $BiVO_4$: elucidating the role of the Bi s and V d orbitals. *Chem. Mater.* **2009**, *21*, 547−551.
(31) Cooper, J. K.; Gul, S.; Toma, F. M.; Chen, L.; Liu, Y. S.; Guo, J.; Ager, J. W.; Yan, J.; Sharp, I. D. Indirect bandgap and optical properties of monoclinic bismuth vanadate. *J. Phys. Chem. C* **2015**, *119*, 2969−2974.
(32) Ding, K.; Chen, B.; Fang, Z.; Zhang, Y. Density functional theory study on the electronic and optical properties of three crystalline phases of $BiVO_4$. *Theor. Chem. Acc.* **2013**, *132*, No. 1352.
(33) Zhao, Z.; Li, Z.; Zou, Z. Electronic structure and optical properties of monoclinic clinobisvanite $BiVO_4$. *Phys. Chem. Chem. Phys.* **2011**, *13*, 4746−4753.
(34) Ma, J.; Wang, L.-W. The role of the isolated 6s states in $BiVO_4$ on the electronic and atomic structures. *Appl. Phys. Lett.* **2014**, *105*, No. 172102.
(35) Yi, J.; Zhao, Z. Y.; Wang, Y. A.; Zhou, D. C.; Ma, C. S.; Cao, Y. C.; Qiu, J. B. Monophasic zircon-type tetragonal $Eu_{1-x}Bi_xVO_4$ solid-solution: synthesis, characterization, and optical properties. *Mater. Res. Bull.* **2014**, *57*, 306−310.
(36) Kudo, A. Z-scheme photocatalyst systems for water splitting under visible light irradiation. *MRS Bull.* **2011**, *36*, 32−38.
(37) Wang, Q.; Liu, H.; Yuan, J.; Shangguan, W. F. Synthesis and characterization of visible-light-responding $Bi_{0.5}La_{0.5}VO_4$ solid solution for photocatalytic water splitting. *Chin. J. Catal.* **2009**, *30*, 565−569.
(38) Wang, Q.; Liu, H.; Jiang, L.; Yuan, J.; Shangguan, W. F. Visible-light-responding $Bi_{0.5}Dy_{0.5}VO_4$ solid solution for photocatalytic water splitting. *Catal. Lett.* **2009**, *131*, 160−163.
(39) Wang, Q.; Jiang, L.; Liu, H.; Yuan, J.; Chen, M. X.; Shi, J. W.; Shangguan, W. F. Preparation and characterization of $Bi_{1-x}Gd_xVO_4$ photocatalyst and its application to water splitting. *Acta Phys.-Chim. Sin.* **2009**, *25*, 1703−1707.
(40) Wang, Q.; An, N.; Mu, R. J.; Liu, H.; Yuan, J.; Shi, J. W.; Shangguan, W. F. Photocatalytic water splitting by band-gap engineering of solid solution $Bi_{1-x}Dy_xVO_4$ and $Bi_{0.5}M_{0.5}VO_4$ (M = La, Sm, Nd, Gd, Eu, Y). *J. Alloys Compd.* **2012**, *522*, 19−24.
(41) Xu, H.; Wu, C. D.; Li, H. M.; Chu, J. Y.; Sun, G. S.; Xu, Y. G.; Yan, Y. S. Synthesis, characterization and photocatalytic activities of rare earth-loaded $BiVO_4$ catalysts. *Appl. Surf. Sci.* **2009**, *256*, 597−602.
(42) Luo, Y. Y.; Tan, G. Q.; Dong, G. H.; Ren, H. J.; Xia, A. A comprehensive investigation of tetragonal Gd-doped $BiVO_4$ with enhanced photocatalytic performance under sun-light. *Appl. Surf. Sci.* **2016**, *364*, 156−165.
(43) Adán, C.; Marugan, J.; Obregon, S.; Colon, G. Photocatalytic *Escherichia coli* inactivation by means of trivalent Er^{3+}, Y^{3+} doping of $BiVO_4$ system. *Appl. Catal., A* **2016**, *526*, 126−131.
(44) Yi, J.; Zhao, Z. Y.; Wang, Y. A. Systematic studies on $Yb_xBi_{1-x}VO_4$:Tm^{3+} solid solutions: experiments and DFT calculations on up-conversion photoluminescence properties. *RSC Adv.* **2018**, *8*, 596−605.
(45) Huang, H.; Wang, Z.; Huang, B.; Wang, P.; Zhang, X.; Qin, X.; Dai, Y.; Zhu, G.; Whangbo, M. H. Intense single red emission induced by near-infrared irradiation using a narrow bandgap oxide $BiVO_4$ as the host for Yb^{3+} and Tm^{3+} ions. *Adv. Opt. Mater.* **2018**, *6*, No. 1701331.
(46) Regmi, C.; Kshetri, Y. K.; Ray, S. K.; Pandey, R. P.; Lee, S. W. Utilization of visible to NIR light energy by Yb^{+3}, Er^{+3} and Tm^{+3} doped $BiVO_4$ for the photocatalytic degradation of methylene blue. *Appl. Surf. Sci.* **2017**, *392*, 61−70.
(47) Liu, T.; Tan, G. Q.; Zhao, C. C.; Xu, C.; Su, Y. N.; Wang, Y.; Ren, H. J.; Xia, A.; Shao, D.; Yan, S. M. Enhanced photocatalytic mechanism of the Nd-Er co-doped tetragonal $BiVO_4$ photocatalysts. *Appl. Catal., B* **2017**, *213*, 87−96.
(48) Allen, J. P.; Galea, N. M.; Watson, G. W.; Palgrave, R. G.; Kahk, J. M.; Payne, D. J.; Robinson, M. D. M.; Field, G.; Regoutz, A.; Egdell,

DOI: 10.1021/acs.jpcc.8b10573
J. Phys. Chem. C 2019, 123, 8484−8499

R. G. Valence states in $CeVO_4$ and $Ce_{0.5}Bi_{0.5}VO_4$ probed by density functional theory calculations and x-ray photoemission spectroscopy. *J. Phys. Chem. C* **2014**, *118*, 25330−25339.
(49) Cheng, X. R.; Guo, D. J.; Feng, S. Q.; Yang, K.; Wang, Y. Q.; Ren, Y. F.; Song, Y. Structure and stability of monazite- and zircon-type $LaVO_4$ under hydrostatic pressure. *Opt. Mater.* **2015**, *49*, 32−38.
(50) Chakoumakos, B. C.; Abraham, M. M.; Boatner, L. A. Crystal-structure refinements of zircon-type MVO_4 (M = Sc, Y, Ce, Pr, Nd, Tb, Ho, Er, Tm, Yb, Lu). *J. Solid State Chem.* **1994**, *109*, 197−202.
(51) Mullica, D. F.; Sappenfield, E. L.; Abraham, M. M.; Chakoumakos, B. C.; Boatner, L. A. Structural investigations of several $LnVO_4$ compounds. *Inorg. Chim. Acta* **1996**, *248*, 85−88.
(52) Shannon, R. D. Revised effective ionic-radii and systematic studies of interatomic distances in halides and chalcogenides. *Acta Crystallogr., Sect. A: Cryst. Phys., Diffr., Theor. Gen. Crystallogr.* **1976**, *32*, 751.
(53) Bhattacharya, A. K.; Mallick, K. K.; Hartridge, A. Phase transition in $BiVO_4$. *Mater. Lett.* **1997**, *30*, 7−13.
(54) Yeh, J. J.; Lindau, I. Atomic subshell photoionization cross-sections and asymmetry parameters: $1 \leq Z \leq 103$. *At. Data Nucl. Data Tables* **1985**, *32*, 1−155.
(55) Cox, P. A.; Baer, Y.; Jorgensen, C. K. Coefficients of fractional parentage for ionization of partly filled f-shells compared with photoelectron spectra of lanthanide compounds and metals. *Chem. Phys. Lett.* **1973**, *22*, 433−438.
(56) Cox, P. A.; Lang, J. K.; Baer, Y. Study of the 4f and valence band density of states in rare-earth-metals.1. Theory of the 4f states. *J. Phys. F: Met. Phys.* **1981**, *11*, 113−119.
(57) Gerken, F. Calculated photoemission spectra of the 4f states in the rare-earth-metals. *J. Phys. F: Met. Phys.* **1983**, *13*, 703−713.
(58) Beatham, N.; Cox, P. A.; Orchard, A. F.; Grant, I. P. Final-state intensities in photoelectron-spectra of 4f electrons as predicted by relativistic calculations. *Chem. Phys. Lett.* **1979**, *63*, 69−71.
(59) Orchard, A. F.; Thornton, G. Study of final-state structure in XPE spectra of rare-earth-oxides. 2. Ionization of a 4f electron. *J. Electron Spectrosc. Relat. Phenom.* **1977**, *10*, 1−14.
(60) Holm, A. P.; Ozawa, T. C.; Kauzlarich, S. M.; Morton, S. A.; Waddill, G. D.; Tobin, J. G. X-ray photoelectron spectroscopy studies of $Yb_{14}MnSb_{11}$ and $Yb_{14}ZnSb_{11}$. *J. Solid State Chem.* **2005**, *178*, 262−269.
(61) Machida, M.; Murakami, S.; Kijima, T.; Matsushima, S.; Arai, M. Photocatalytic property and electronic structure of lanthanide tantalates, $LnTaO_4$ (Ln = La, Ce, Pr, Nd, and Sm). *J. Phys. Chem. B* **2001**, *105*, 3289−3294.
(62) Taverner, A. E.; Rayden, C.; Warren, S.; Gulino, A.; Cox, P. A.; Egdell, R. G. A comparison of the energies of vanadium donor levels in doped SnO_2 and TiO_2. *Phys. Rev. B* **1995**, *51*, 6833−6837.
(63) Egdell, R. G.; Gulino, A.; Rayden, C.; Peacock, G.; Cox, P. A. On the nature of donor states in V-doped SnO_2. *J. Mater. Chem.* **1995**, *5*, 499−504.
(64) Briggs, D.; Seah, M. P. *Practical Surface Analysis*; John Wiley: Chichester, 1994.
(65) Burroughs, P.; Hamnett, A.; Orchard, A. F.; Thornton, G. Satellite structure in x-ray photoelectron-spectra of some binary and mixed oxides of lanthanum and cerium. *J. Chem. Soc., Dalton Trans.* **1976**, 1686−1698.
(66) Suzuki, C.; Kawai, J.; Takahashi, M.; Vlaicu, A. M.; Adachi, H.; Mukoyama, T. The electronic structure of rare-earth oxides in the creation of the core hole. *Chem. Phys.* **2000**, *253*, 27−40.
(67) Kotani, A.; Ogasawara, H. Theory of core-level spectroscopy of rare-earth-oxides. *J. Electron Spectrosc. Relat. Phenom.* **1992**, *60*, 257−299.
(68) Nakano, T.; Kotani, A.; Parlebas, J. C. Theory of XPS and BIS spectra in Ce_2O_3 and CeO_2. *J. Phys. Soc. Jpn.* **1987**, *56*, 2201−2210.
(69) Fujimori, A. Mixed-valent ground-state of CeO_2. *Phys. Rev. B* **1983**, *28*, 2281−2283.
(70) Fujimori, A. Spectroscopic evidence for localized and extended f-symmetry states in CeO_2 - comment. *Phys. Rev. Lett.* **1984**, *53*, 2518.
(71) Kotani, A.; Mizuta, H.; Jo, T.; Parlebas, J. C. Theory of core photoemission spectra in CeO_2. *Solid State Commun.* **1985**, *53*, 805−810.
(72) Thornton, G.; Dempsey, M. J. Final-state effects in the 3d and 4d X-ray photoelectron-spectra of CeO_2. *Chem. Phys. Lett.* **1981**, *77*, 409−412.
(73) Bianconi, A.; Miyahara, T.; Kotani, A.; Kitajima, Y.; Yokoyama, T.; Kuroda, H.; Funabashi, M.; Arai, H.; Ohta, T. Correlation satellites in deep metal 3p core x-ray photoemission of tetravalent oxides CeO_2, PrO_2, TbO_2, HfO_2 and of LaF_3. *Phys. Rev. B* **1989**, *39*, 3380−3385.
(74) Bianconi, A.; Kotani, A.; Okada, K.; Giorgi, R.; Gargano, A.; Marcelli, A.; Miyahara, T. Many-body effects in praseodymium core-level spectroscopies of PrO_2. *Phys. Rev. B* **1988**, *38*, 3433−3437.
(75) Cohen, O.; Potter, F. H.; Rastomjee, C. S.; Egdell, R. G. A core and valence level photoemission-study of $Y_{1-x}Pr_xBa_2Cu_3O_7$. *Phys. C* **1992**, *201*, 58−68.
(76) Felner, I.; Yeshurun, Y.; Hilscher, G.; Holubar, T.; Schaudy, G.; Yaron, U.; Cohen, O.; Wolfus, Y.; Yacoby, E. R.; Klein, L.; et al. Crystal structure, magnetic properties, x-ray-photoemission-spectroscopy, and specific-heat measurements on Pr_2BaO_4 and $PrBaO_3$. *Phys. Rev. B* **1992**, *46*, 9132−9141.
(77) Kotani, A.; Ogasawara, H. Interplay between intra-atomic multiplet coupling and interatomic hybridization in core-level spectroscopy. *J. Electron Spectrosc. Relat. Phenom.* **1997**, *86*, 65−72.
(78) Pembamabiala, J. M.; Lenzi, M.; Lenzi, J.; Lebugle, A. XPS study of mixed cerium terbium orthophosphate catalysts. *Surf. Interface Anal.* **1990**, *15*, 663−667.
(79) Hagström, S. B.; Heden, P. O.; Lofgren, H. Electron density of states in Yb metal as observed by X-ray photoemission. *Solid State Commun.* **1970**, *8*, 1245−1248.
(80) Park, K. W.; Ahn, S.; Lim, S. H.; Jin, M. H.; Song, J.; Yun, S. Y.; Kim, H. M.; Kim, G. J.; Ok, K. M.; Hong, J. Ytterbium oxide nanodots via block copolymer self-assembly and their efficacy to dye-sensitized solar cells. *Appl. Surf. Sci.* **2016**, *364*, 573−578.
(81) Orchard, A. F.; Thornton, G. Study of final-state structure in XPE spectra of rare-earth oxides.3. Ionization of a 4d electron. *J. Electron Spectrosc. Relat. Phenom.* **1978**, *13*, 27−38.
(82) Henderson, B.; Imbusch, G. F. *Optical Spectroscopy of Inorganic Solids*; Clarendon Press: Oxford, 2006.
(83) Prokofiev, A. V.; Shelykh, A. I.; Melekh, B. T. Periodicity in the band gap variation of Ln_2X_3 (X = O, S, Se) in the lanthanide series. *J. Alloys Compd.* **1996**, *242*, 41−44.
(84) Medenbach, O.; Dettmar, D.; Shannon, R. D.; Fischer, R. X.; Yen, W. M. Refractive index and optical dispersion of rare earth oxides using a small-prism technique. *J. Opt. A: Pure Appl. Opt.* **2001**, *3*, 174−177.
(85) Yuan, Y.; Huang, Y. H.; Ma, F.; Zhang, Z. Q.; Wei, X. M. Effects of oxygen vacancy on the mechanical, electronic and optical properties of monoclinic $BiVO_4$. *J. Mater. Sci.* **2017**, *52*, 8546−8555.

DOI: 10.1021/acs.jpcc.8b10573
J. Phys. Chem. C 2019, 123, 8484−8499